ELSEVIER

Contents lists available at ScienceDirect

Acta Materialia

journal homepage: www.elsevier.com/locate/actamat



Full length article

Modelling the Bauschinger effect in copper during preliminary load cycles

Alvaro Martinez-Pechero ^{a,b}, Eralp Demir ^a, Chris Hardie ^b, Yevhen Zayachuk ^b, Anna Widdowson ^b, Edmund Tarleton ^a

- a Department of Engineering Science, University of Oxford, Parks road, Oxford OX1 3PJ, UK
- b UK Atomic Energy Authority, Culham Centre for Fusion Energy, Oxfordshire, UK

ARTICLE INFO

Keywords:
Crystal plasticity
Bauschinger effect
Copper
Armstrong-frederick model
Voce-type hardening
Orowan-sleeswyk model
GND

ABSTRACT

This research utilizes established cyclic deformation models to simulate the Bauschinger effect observed in copper monocrystal cantilever experiments during the initial bending and straightening phases. Crystal plasticity finite element simulations employing *Armstrong-Frederick, Orowan-Sleeswyk*, and various other backstress models have drawbacks to reproduce the experimental force–displacement curves accurately since they are not able to reproduce the isotropic hardening measured during cantilever straightening. However, the *Armstrong-Frederick* model combined with *Voce-type hardening* and a newly proposed *modified Orowan-Sleeswyk* model has proven to be effective. In this work, we propose a *modified Orowan-Sleeswyk* model, based on recent studies, where not all the geometrically necessary dislocations (GND) recombine during the straightening phase, but instead reorient to achieve a net zero-strain gradient with ongoing hardening during load reversal.

1. Introduction

Copper has excellent thermal conductivity and adequate mechanical strength for high thermal stresses, therefore it is often used as a stress-relieving interlayer at the bond interface between the radiation shield and the heat sink in plasma-facing components (PFC) of fusion reactors such as Wendelstein-7X, JET, and ITER [1,2]. Cyclic high-heat-flux loads caused by pulsed plasma operations generate a repeated variation in thermal stress in the PFC structure. Under these circumstances, the copper bond layer experiences alternating loads that cause plastic strain accumulation responsible for hardening during deformation (expansion or contraction) or softening when the sense of deformation changes (from expansion to contraction or vice-versa), leading to cycle fatigue of the material [2].

The Bauschinger effect refers to the reduction in yield strength observed when the direction of the applied load is reversed or when the load path is changed [3]. For cyclic deformations, it could explain stress saturation at relatively low stresses, frequently forming persistent slip bands (PSBs) due to extrusions/intrusions that can lead to fatigue cracks [4]. In polycrystals, this effect is well understood and is mainly attributed to polarized dislocations in front of the crystal grain boundaries, as supported by experimental evidence [5,6].

In single-crystals, the dislocation structures responsible are still under debate [5]. Currently, there are two main explanations for the Bauschinger effect. The first involves cells formed by dislocations that produce long-range internal stresses (LRIS). This phenomenon

was first studied by Mughrabi [7] and Pedersen [8] who proposed a structure called dislocation cell, formed of regions with high yield stress/dislocation densities (cell walls) in combination with lower yield stress/dislocation densities regions (cell interiors); this structure remains nearly invariable during cycles. The second is based on complex distributions of dislocation obstacles that allow movement of dislocations in one direction but not in others until high strain levels are produced [9.10].

This discussion has remained open for several years, Kassner et al. [11] support the idea of cell structures based on compression and tension experiments on monocrystals of copper, nickel and aluminium but noted that the LRIS were smaller than initially expected and did not discard the idea of the *Orowan-Sleeswyk model*. Levine et al. [4] worked with the compression of monocrystal copper micropillars, measuring low LRIS associated with cell structures and concluding that both models (*Mughrabi* and *Orowan-Sleeswyk*) have importance. The discussion is more complex when we have curvature as during cantilever experiments. The lattice curvature allows the formation of geometrically necessary dislocations (GND) that increase the impact of the *Orowan-Sleeswyk* model. In addition, the interaction of the curvature with extrusions or intrusions in the metal creates slip bands that act as obstacles to the dislocations and are particularly complex to model during the first load cycles [5,12].

^{*} Corresponding author at: Department of Engineering Science, University of Oxford, Parks road, Oxford OX1 3PJ, UK. *E-mail address:* alvaro.martinezpechero@eng.ox.ac.uk (A. Martinez-Pechero).

On the other hand, other models have appeared such as Armstrong-Frederick model and its variations [13,14], that are not based on dislocations like the two previous ones (Mughrabi and Orowan-Sleeswyk). These models are based on crystal slip, a much simpler quantity to calculate, reducing the computation time and complexity. They have been widely used in the literature for polycrystals [15,16] and monocrystals [17]. They have also been used in combination with the Orowan-Sleeswyk model in [18] but in this case, an equation with the same structure as the Armstrong-Frederick model is used to model the isotropic hardening (non-softening) and the Orowan-Sleeswyk model is responsible for the Bauschinger effect.

Recent studies indicate that the Bauschinger effect and hardening are different during initial load cycles of cantilever experiments [19, 20]. In these studies, a monocrystal copper cantilever undergoes load and straightening cycles. The results showed a more pronounced Bauschinger effect than in polycrystal copper or monocrystal after many cycles, furthermore, isotropic hardening occurred between cycles. Consequently, Ugi et al. [20] illustrates the evolution of GND in a cantilever experiment during initial cycles. The GND distribution contradicts the idea that the structure of the dislocation cell remains constant throughout the full bending/straightening cycle. The GND pile-ups formed during the first bending are converted to a highly complex structure during the straightening, with the dislocation density being distributed throughout the cantilever base giving rise to the isotropic hardening. Dislocation dynamics simulations provide qualitative information [21], but are computationally expensive for cantilever experiments, making crystal plasticity codes a more practical approach to modelling these types of experiments [22].

In Demir et al. [19], it is exposed the results of a Bauschinger experiment using a single-crystal copper cantilever. Based on these experimental results, this study has modelled the Bauschinger effect during initial bending/straightening cycles, comparing the results between two well-known types of model: Armstrong-Frederick [13] combined with hardening laws and GND-based models [9].

The modelling process used the OXFORD-UMAT code [23] (code available on [24]), which was designed to analyse various types of materials for the Spherical Tokamak for Energy Production reactor. The code incorporates models for plasticity, GND calculus and hardening. The GND calculations follow the method proposed by Demir et al. [22].

2. Cantilever experiment

Demir et al. [19] studied the Bauschinger effect [3] of a monocrystal copper cantilever ($25.4 \times 8.64 \times 7.05 \mu m$, Fig. 1(b)) consisting of three total cycles of bending and straightening.

The cantilever was produced from a single-crystal copper sample grown in a Bridgman furnace. First, a cylindrical sample with a diameter of 100 μm was crafted using wire electro-discharge grinding and subsequently etched in a 40% HNO3 solution. Finally, focused ion beam (FIB) milling shaped the cantilever beam from this cylindrical specimen, using a 500 pA current at 30 keV to finish all surfaces [19]. The initial Euler angles [25] were $\phi_1 = 260.0^\circ$, $\Phi = 101.1^\circ$, $\phi_2 = 248.2^\circ$ and the corresponding Miller indices were [5 $\bar{2}$ $\bar{1}$] for the longitudinal beam axis (z-axis), [$\bar{4}$ $\bar{1}$ 2] for the transverse direction (y-axis), and [5 2 21] for the loading axis (x-axis) as shown in Fig. 1(b).

The cantilever was bent by a Hysitron $^{\mathbb{R}}$ indenter with a spherical indenter that produced a displacement of 3 μm at a speed of 1 μm s $^{-1}$ in displacement-controlled mode. The indentation region was situated at a distance of 17.3 μm from the base. The size of the indented region (approximately 2 μm^3) was much smaller than the bent volume (approximately 180 μm^3), having only a small influence on the strength of the cantilever during deformation.

The bending and straightening process consists of three stages in each cycle: (i) the indenter bends the cantilever (bending), (ii) the indenter stops applying pressure and gradually releases the load to zero

(unloading), and (iii) the cantilever is loaded in the reverse direction until it is straightened to its original position (straightening).

Fig. 1(a) illustrates the force–displacement measurements of the experiments in the first three consecutive cycles. There is a notable increase in hardening during bending in successive cycles. There are also drops in force during the 1st bending, which appear as discontinuities in the blue line. These drops are attributed to the formation of slip bands (see slip bands in Fig. 1(b)), which cause a plastic displacement of the cantilever with less resistance than usual. Once formed, these slip bands act as obstacles to dislocations, contributing to increase the hardening [12].

During the straightening process, the yield strength is significantly lower than the yield strength observed during bending. Demir et al. [19] estimates a stress reduction of 73% (1st cycle), 76% (2nd cycle) and 83% (3rd cycle) relative to the bending yield stress. This observed reduction in the yield strength during straightening is due to internal backstresses that support the load reversal. They arise from sets of GND accumulated during forward bending that disappear (through the glide in the reverse direction which causes the annihilation with dislocations of the opposite sign) as the cantilever returns to the original position.

3. Crystal plasticity framework

A detailed description of the crystal plasticity simulation code used in this study (OXFORD-UMAT) can be found in [23]. The code was applied in combination with the finite element software Abaqus [26], while the specific methodology for GND calculation is outlined in [22]. This section presents an overview of the crystal plasticity kinematics and constitutive laws governing slip behaviour in the material.

3.1. Crystal plasticity kinematics

The deformation gradient in a crystal under stress can be defined by $F_{tot} = F_e F_p$, where F_e is the mechanical elastic deformation gradient, F_p the plastic deformation gradient.

The mechanical elastic deformation gradient F_e is calculated using the Jaumann stress rate [27] and a method (explained in [23]) which uses the total deformation components minus the plastic deformation components.

The plastic deformation gradient F_p is calculated from the plastic velocity gradient L_p , which is the sum of the slip rates $\dot{\gamma}^a$ times the Schmid tensor S^a of each slip system a , which is the dyadic product $s^a \otimes n^a$, where s^a is the slip direction and n^a the slip plane normal of the plastically deformed lattice [28]:

$$L_{p} = \dot{F}_{p} F_{p}^{-1} = \sum_{a} \dot{\gamma}^{a} s^{a} \otimes n^{a} = \sum_{a} \dot{\gamma}^{a} S^{a}. \tag{3.1}$$

However, the slip system undergoes elastic deformations, transforming the slip and normal direction to a deformed configuration (n_a^a, s_a^a) :

$$s_e^a = F_e s^a; \quad n_e^a = F_e^{-T} n^a = n^a F_e^{-1}.$$
 (3.2)

The rotation, g, is applied to use the experiment reference frame during calculations (Bunge convention), where ϕ_1 , Φ , and ϕ_2 represent the Euler angles [29], for further details see Appendix A. The temporal evolution of the crystal orientation is computed by updating g from an initial time t to a subsequent time $t+\Delta t$, where Δt represents the discrete time increment. This update can be expressed as:

$$\mathbf{g}_{t+\Delta t} = \mathbf{g} = (\mathbf{I} + \Delta \mathbf{\Omega}_e \, \Delta t) \, \mathbf{g}_t. \tag{3.3}$$

Using the orientation rates according to [30]: $\dot{g} = \Delta \Omega_e \, g$. In which $\Delta \Omega_e$ is the elastic spin obtained by subtracting the plastic spin from the total spin:

$$\Delta\Omega_{e} = \Delta\Omega - \Delta\Omega_{p}; \begin{cases} \Delta\Omega_{p} = \sum_{a} W^{a} \dot{\gamma}^{a} \\ \Delta\Omega = \frac{L - L^{T}}{2} \end{cases}$$
(3.4)

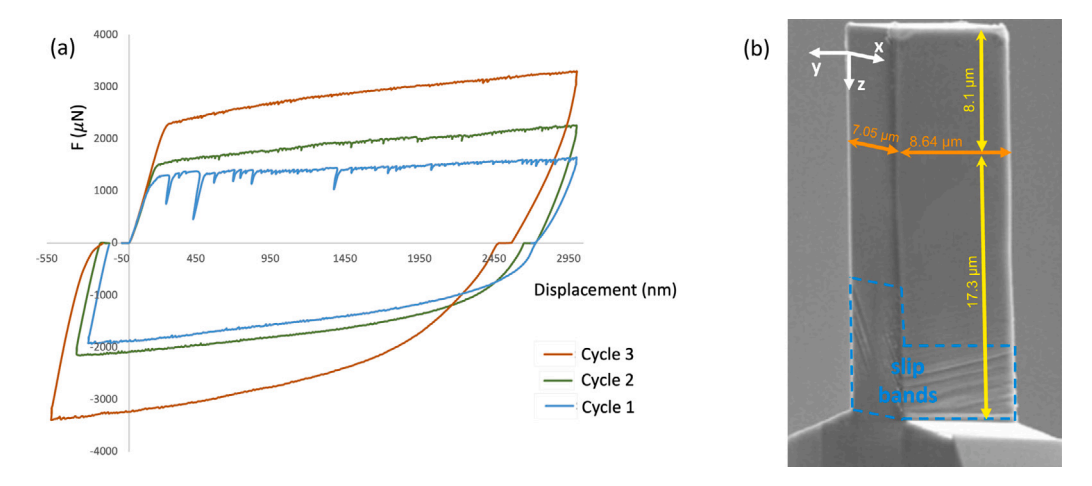


Fig. 1. (a) Force-displacement bending and straightening cycles of the cantilever experiment [19]. The plateaus observed at 0 μ N in the force-displacement curves correspond to the retraction phase of the indenter, during which it disengages from the copper cantilever. Consequently, these regions do not reveal meaningful data regarding the mechanical properties of the copper specimen. (b) SEM image of the experiment at end of the first bending straightening cycle, indicating the dimensions of the cantilever. The distances from the base and the top of the cantilever where the indenter was applied are shown in yellow. The areas with slip bands created by active slip systems are shown in blue. (For interpretation of the references to colour in this figure legend, the reader is referred to the web version of this article.)

$$\mathbf{W}^{a} = \frac{1}{2} \left(s_{e}^{a} \otimes \mathbf{n}_{e}^{a} - \mathbf{n}_{e}^{a} \otimes s_{e}^{a} \right). \tag{3.5}$$

Where W^a is the antisymmetric matrix of the Schmid tensor, and $\dot{\gamma}^a$ is the slip rate, which is determined by various plastic models. L is the velocity gradient of the total strain, defined by $L = \dot{F} F^{-1}$.

The set of equations is solved through a semi-implicit algorithm implemented in a user-defined material subroutine (OXFORD-UMAT [23]) for the finite element software Abaqus, which uses the Foward-Gradient algorithm [31] to obtain the approximate initial and backup solution for the Cauchy stress.

3.2. Constitutive laws

The constitutive laws depend on the elasticity and the slip rate responsible for the plasticity (Eq. (3.1)). Elasticity relates the rotation-free objective Jaumann rate of stress, σ [32], to the vectorized form of elastic deformation rate d_e , writing the 4th rank elasticity tensor $\mathbb C$ for the deformed configuration [33] in Voigt notation:

$$\overset{\nabla}{\sigma} = \mathbb{C} : d_e; \quad \mathbb{C} = R \, \mathbb{C}_0 \, R^T \tag{3.6}$$

where $\mathbb C$ is a 6 \times 6 matrix obtained by applying the rotation matrix R to the elastic stiffness constant $\mathbb C_0$ [34], thus adjusting it from the crystalline reference to the experimental one (see Appendix B). The stiffness constant $\mathbb C_0$ for a face-centered cubic material (FCC) such as copper is given by three elastic constants C_{11} , C_{12} , C_{44} [35]

The slip rates of the slip system "a" are calculated using the hyperbolic-sine law [36], where α and β were assumed to be constants adjusted according to [35], τ_{eff}^a is the effective resolved shear stress (RSS) in each slip system, and τ_c^a the critical resolved shear stress (CRSS), which depends on the initial *Statistically Stored Dislocations* (SSD) density and needs to be calibrated:

$$\dot{\gamma}^{a} = \alpha \sinh(\beta \left(\left| \tau_{eff}^{a} \right| - \tau_{c}^{a} \right)) \operatorname{sign}(\tau_{eff}^{a})$$
(3.7)

in which the effective RSS is given by the RSS, τ^a , minus the backstress term, χ^a :

$$\tau^a_{eff} = \tau^a - \chi^a. \tag{3.8}$$

The prefactors of the slip law are computed based on physical parameters according to:

$$\alpha = \rho_m b^2 v_0 \exp\left(-\frac{\Delta F}{K_B T}\right); \quad \beta = \frac{\Delta V^a}{K_B T}. \tag{3.9}$$

The model parameters for crystal orientation, elastic constants, and the slip law are given in the table below:

Parameter	Definition	Unit	Value [35]
ϕ_1	Undeformed euler angle 1	Degrees	260
Φ	Undeformed euler angle 2	Degrees	101.1
ϕ_2	Undeformed euler angle 3	Degrees	248.2
C_{11}	Elastic constant 1	MPa	$168 \cdot 10^3$
C_{12}	Elastic constant 2	MPa	$121.4 \cdot 10^3$
C_{44}	Elastic constant 3	MPa	$75.4 \cdot 10^3$
α	Constant value	1/s	10^{-5}
β	Constant value	1/MPa	0.2
ΔF	Activation energy for slip	eV	0.5
ν_0	Attempt frequency	1/s	10^{11}
ΔV	Activation volume	b^3	50
b	Burgers vector	μm	$2.56 \cdot 10^{-4}$
$ ho_m$	Mobile dislocation density	μm^{-2}	0.5
K_B	Boltzmann constant	$eV K^{-1}$	$8.61 \cdot 10^{-5}$
T	Temperature	K	300

4. GND model

Heterogeneity in crystal deformation causes the formation of the *Geometrically Necessary Dislocations* (GND) responsible of hardening and backstress (lower yield strength when cantilever straightening) [9,37].

GND density (ϱ_{GND}) [38] is the sum of the length of dislocations per unit volume that is obtained by the lattice incompatibility in the crystalline structure. GND density is calculated according to the formula [39]:

$$\begin{split} \boldsymbol{\Lambda} &= - \left(\nabla \times \boldsymbol{F}_{p} \right)^{T} = \sum_{a} \rho_{GND}^{a} b^{a} s^{a} \otimes \boldsymbol{I}^{a} \\ &= \sum_{a} \left(\rho_{GND,edge}^{a} b^{a} s^{a} \otimes \boldsymbol{t}^{a} + \rho_{GND,screw}^{a} b^{a} s^{a} \otimes s^{a} \right) \end{split} \tag{4.1}$$

where Λ is the Nye tensor that represents lattice incompatibility, b^a is the length of the Burgers vector of the slip system a, I^a is the dislocation line. Note that the line direction is the slip direction s^a , and transverse direction t^a , for screw and edge dislocations, respectively.

GND density was calculated from the lattice incompatibility in Eq. (4.1) considering only active slip systems and using generalized singular value decomposition to solve the system [22].

5. Modelling Bauschinger effect

Various models have been proposed based on slip γ or GND to model the Bauschinger effect [4,7,9,13,20], (see scheme in Fig. 2).

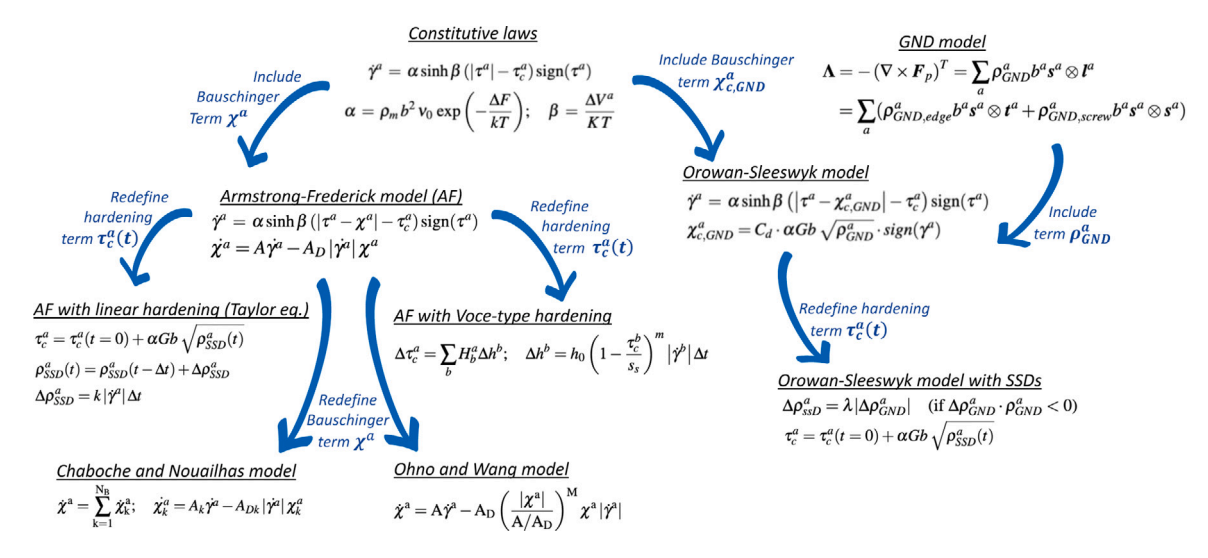


Fig. 2. Scheme of the models analysed in this study.

5.1. Armstrong-Frederick model

The Armstrong-Frederick (A-F) model is a phenomenological model that integrates the concepts of proportional hardening and saturation into the backstress term χ^a in Eq. (3.8), providing greater precision during cyclic loading:

$$\chi^{\dot{a}} = A\gamma^{\dot{a}} - A_D \left| \gamma^{\dot{a}} \right| \chi^a \tag{5.1}$$

where χ^a represents the backstress rate, γ^a is the slip rate, A and A_D are parameters associated with direct hardening and dynamic recovery respectively that need to be adjusted [18]. The backstress χ^a evolves quasi-linear at the beginning of deformation, curving progressively until a saturation value of A/A_D .

The *A-F* model was first applied to crystal plasticity by [40] and was later adopted by other researchers in their own crystal plasticity frameworks. Several variations have been proposed, such as the *Chaboche* model (Eq. (5.2)) [41] that introduced a combination of linear and non-linear hardening terms or the *Ohno-Wang* model (Eq. (5.3)) [42]:

$$\dot{\chi}^{a} = \sum_{k=1}^{N_{\mathrm{B}}} \dot{\chi}_{k}^{a}; \quad \dot{\chi}_{k}^{a} = A_{k} \dot{\gamma}^{a} - A_{Dk} \left| \dot{\gamma}^{a} \right| \chi_{k}^{a}$$

where $A_{Dk} = 0$ for only linear hardening terms. (5.2)

$$\dot{\chi}^{a} = A\dot{\gamma}^{a} - A_{D} \left(\frac{|\chi^{a}|}{A/A_{D}} \right)^{M} \chi^{a} \left| \dot{\gamma}^{a} \right|. \tag{5.3}$$

All these models are empirical and were applicable to the macroscopic length scale to capture the Bauschinger effect and cyclic ratcheting, but they are not expected to capture the underlying mechanisms at a lower length-scale [18]. Section 6.1 demonstrates how these models present important limitations to capture the level of observed hardening during the first cycles of deformation [19]. To overcome this limitation, we combine *A-F type* models with *linear SSD hardening* or *Voce-type hardening* models that include isotropic hardening during bending and straightening without contributing to backstress.

5.1.1. A-F combined with linear SSD hardening

The critical resolved shear stress (CRSS) is defined by Taylor relation (Eq. (5.4)) [37] that depends on the dislocations density in which τ_c^0 is the initial strength or friction stress:

$$\tau_c^a = \tau_c^0 + \alpha G b \sqrt{\rho_{SSD}^a}. \tag{5.4}$$

The evolution of *statistically stored dislocation (SSD)* density is given by [36]:

$$\dot{\varrho}_{SSD}^a = k \ |\dot{\gamma}^a| \tag{5.5}$$

where τ_c^a is the CRSS on slip system a, ρ_{SSD}^a is the SSD density, G is the shear modulus, α and k are geometrical parameters being $\alpha = 0.25$ and k needs to be adjusted.

5.1.2. A-F combined with voce-type hardening

Voce-type hardening [43,44] is an experimentally-based hardening model composed of a hardening rate and a saturation term. It also considers latent hardening interactions between slip systems:

$$\Delta \tau_c^a = \sum_b H_b^a \Delta h^b; \quad \Delta h^b = h_0 \left(1 - \frac{\tau_c^b}{s_s} \right)^m \left| \dot{\gamma}^b \right| \Delta t \tag{5.6}$$

where h_0 is the hardening rate, s_s is the saturation slip strength that represents the saturation of hardening, m is the hardening exponent and H_b^a is the hardening interaction matrix of the slip system^b in the slip system^a.

In our models, the Voce-type hardening will be used to represent the linear hardening observed experimentally. Given that Demir et al. [19] did not observe any decrease in the hardening during the initial cycles, we assumed $s_s \gg \tau_c^b$ i.e. $\tau_c^b/s_s \approx 0$, simplifying the expression to:

$$\Delta \tau_c^a = \sum_b H_b^a \Delta h^b; \quad \Delta h^b = h_0 \left| \dot{\gamma}^b \right| \Delta t. \tag{5.7}$$

5.2. Orowan-Sleeswyk model

The *Orowan-Sleeswyk* model [9,10] proposes a Taylor's hardening relation to represent the kinematic hardening produced by GND:

$$\chi^a = C_d \cdot \alpha G b \sqrt{\varrho_{GND}^a} \cdot P^{aa} \cdot \mathrm{sign}(\dot{\gamma^a}) = C_d \cdot \alpha G b \sqrt{\varrho_{GND}^a} \cdot \mathrm{sign}(\gamma^a) \quad (5.8)$$

where $P^{aa}=\mathrm{sign}(\dot{\gamma^a})\cdot\mathrm{sign}(\gamma^a)$, C_d denotes a geometric factor that requires adjustment, $\alpha=0.25$ is a geometrical factor, G the shear modulus, b the Burgers vector magnitude and ρ^a_{GND} the GND density.

 P^{aa} is the reversibility term [45] to determine the sign of χ^a respect to the sign of the resolved shear stress τ^a . P^{aa} is positive (χ^a causes kinematic hardening) when both signs of accumulated slip γ^a and slip rate γ^a are the same, and negative (χ^a causes kinematic softening) otherwise. The overall sign of χ^a is:

$$\operatorname{sign}(\chi^a) = P^{aa} \cdot \operatorname{sign}(\tau^a) = P^{aa} \cdot \operatorname{sign}(\dot{\gamma}^a) = \operatorname{sign}(\dot{\gamma}^a). \tag{5.9}$$

In contrast to the mathematical approach of the *A-F* model, *Orowan-Sleeswyk* model tries to apply our knowledge of dislocation structures. According to Mughrabi et al. [7], two explanations for hardening and softening can be found due to GND. (i) GND obstacles are dislocation cell walls and the hardening results from short-range interactive forces between the walls and the mobile dislocations, while the initial drop

in the yield strength occurs as a consequence of the glide of the GND during the reverse loading, which produces some relaxation of the dislocations cell walls and the plasticity generated in the interior of the cell. (ii) The pile-up of GND in certain regions during deformation causes stress on the slip systems and prevents further slip (strain hardening). For a cantilever, the region corresponds to the neutral axis of the cantilever. During the reverse loading, the backstress induced by the dislocations previously formed facilitates the transition towards equilibrium, contributing to the observed softening.

5.2.1. SSD modification in the Orowan-Sleeswyk model

The examination of load/straightening experimental curves for the cantilever (see Section 2) reveals an excessive increase in hardening during the straightening process, despite the anticipated reduction in yield stress caused by backstress.

HR-ESBD measurements on the monocrystal copper cantilever [20] found the creation of complex dislocation structures, caused by changes in the direction of some of the GND that remain instead of recombining during straightening. In this article, we attribute to these dislocations the excess of hardening generated.

This study proposes to consider these dislocations as responsible for the unexpected hardening observed by [19] during initial cycles. Because developing a dislocation dynamics code to calculate the new orientation of the GND could be complex and computationally expensive, an alternative was to approximate them as randomly oriented and transform these GND into SSD.

$$\Delta \rho_{SSD}^a = \lambda |\Delta \rho_{GND}^a| \quad (\text{if } \Delta \rho_{GND}^a \cdot \rho_{GND}^a < 0)$$
 (5.10)

where $\Delta \rho_{SSD}$ is the change of SSD density, $\Delta \rho_{GND}$ is the change of GND density, λ is the percentage of GND density converted to SSD density. The SSD density increment causes hardening through the Taylor hardening (Eq. (5.4)).

5.3. Finite Element Method (FEM)

The bending and straightening of the above models were simulated using finite element method. The *x*-axis displacement was applied over two lines of nodes on opposite faces of the cantilever at 17.3 μ m from the base (see Fig. 3(a)). The line of nodes were used instead of simulating the indenter to simplify the calculations after finding similar results in the comparative study of Appendix E.

The following boundary conditions were imposed on the model during the successive cycles:

- 1. Bending obtained by displacing the cantilever -3 μ m along the *x*-axis in the indentation region during 3 s (as in Demir et al. [46]).
- 2. 3 s rest by deactivating the load.
- 3. Straightening obtained by displacing the cantilever 3 μm along the x-axis in the opposite direction in the indentation region during 3 s.
- 4. 3 s rest by deactivating the load.

15,600 quadratic tetrahedral elements (C3D20) were applied in simulations. For further details about convergence see Appendix C. The parameters of the Bauschinger models were adjusted using the Nelder–Mead optimization algorithm [47]. The optimization minimizes a distance function between the force–displacement values obtained from experimental data and those derived from simulations [48]. Nelder–Mead was chosen among other optimization methods due to its simplicity of use by not requiring mathematical derivatives of the distance function and its rapid convergence in a limited number of iterations, a crucial factor given the computationally intensive nature of FEM simulations.

The parameter values p_i used to adjust the models are defined by:

$$p_i = \underset{p_i}{\operatorname{arg\,min}} \left(\sum_{cycles} \frac{\int \mid F_{FEM}(u, p_i) - F_{EXP}(u) \mid du}{\int \mid F_{EXP}(u) \mid du} \right)$$
 (5.11)

where F_{FEM} is the force obtained in the model, F_{EXP} is the force measured experimentally, and u is the displacement of the indenter or the displacement of the nodes in the case of the FEM model.

6. Results and discussion

This section presents the results derived from the Bauschinger models applied to the cantilever experiment. The results obtained from the *Armstrong-Frederick* based models are detailed in Section 6.1, while the results from the GND-based models are in Section 6.2.

As mentioned in *Cantilever Experiment* (Section 2), slip bands are formed during the 1st bending due to the activation of dislocation sources [49], but their impact during formation is extremely complex. For this reason, our analysis focuses on the subsequent 2nd and 3rd cycles, where no additional slip bands are created. Once the most suitable models are selected and their parameters adjusted, they will be applied to the 1st cycle trying to estimate the impact associated with the slip bands' formation.

6.1. Armstrong Frederick based models

A-F relate the slip to the hardening and backstress, the accumulated slip γ for a slip system is defined through the Schmid factor and the CRSS (τ_c) of the slip system [28].

Fig. 3(b) shows the initial vector components of the stress during cantilever modelling ($\sigma_z = [\bar{5} \ 2\ 1]$, $\sigma_x = [5\ 2\ 21]$, on crystal coordinates). We can observe how the tensile load σ_z dominates σ_x as we approach the cantilever base (blue zone).

Appendix D includes the table with each slip system (n^a, s^a) , their Schmid factor, and Fig. D.1 shows the accumulated slip γ during the 2nd bending, demonstrating that the main slip activity comes from the two slip systems with the highest Schmid factor, which are shown in more detail in Fig. 4 for the 2nd and 3rd cycle (slip system $(\bar{1}\bar{1}1)[10\bar{1}]$ with Schmid factor 0.49, and slip system $(\bar{1}11)[101]$ with Schmid factor 0.43).

Furthermore, in Fig. 1(b), we can identify two different directions in the slip bands, which seems to confirm the result of our model with two clear main slip systems as responsible for the formation of the hardening and backstress.

Table 6.1 includes the parameters that have been calibrated for the A-F models using the Nelder–Mead optimization algorithm (Section 5.3, Eq. 5.3). Given that copper has a face-centred cubic structure with symmetry in its crystalline lattice, the properties are uniform across the different slip systems. The initial CRSS $\tau_c^0 = 43$ MPa was adjusted to be the same for all models, this value takes into account all the previous hardening suffered in the previous deformation (1st cycle and sample treatment), explaining why it deviates from the values of the literature (19–25 MPa [50]).

Bauschinger model	Hardening model	Parameters adjusted
A-F with saturation (Eq. (5.1))	None	$A = 2050 \text{ MPa s}^{-1},$ $A_D = 30 \text{ s}^{-1}$
A-F with no saturation (Eq. (5.1))	None	$A = 2050 \text{ MPa s}^{-1},$ $A_D = 0 \text{ s}^{-1}$
A-F (Eq. (5.1))	Linear (Eq. (5.5))	$A = 1030 \text{ MPa s}^{-1},$ $A_D = 25 \text{ s}^{-1},$ $k = 1970 \mu\text{m}^{-2}$
A-F with no saturation (Eq. (5.1))	Voce-type (Eq. (5.7))	$A = 1150 \text{ MPa s}^{-1},$ $h_0 = 400 \text{ MPa},$ $A_D = 0 \text{ s}^{-1}, \tau_c^b/s_s = 0$

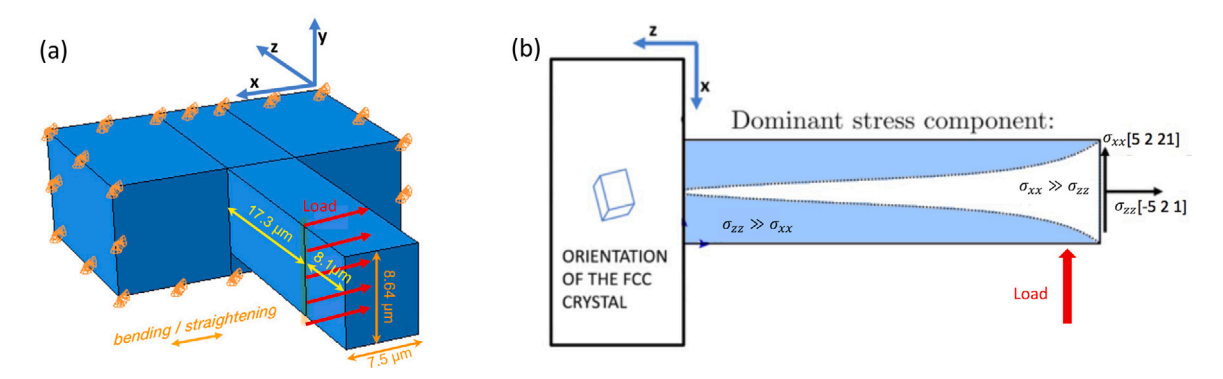


Fig. 3. (a) Boundary conditions for the FEM model during bending/straightening (in yellow, distances from the base and the top of the cantilever where the indenter was applied, in orange, dimensions of the base, in green, line of nodes where the load was applied, in red, direction of the load). (b) Diagram showing load orientation in FCC crystal coordinates. The dominant stress component along the cantilever is also indicated in blue. (For interpretation of the references to colour in this figure legend, the reader is referred to the web version of this article.)

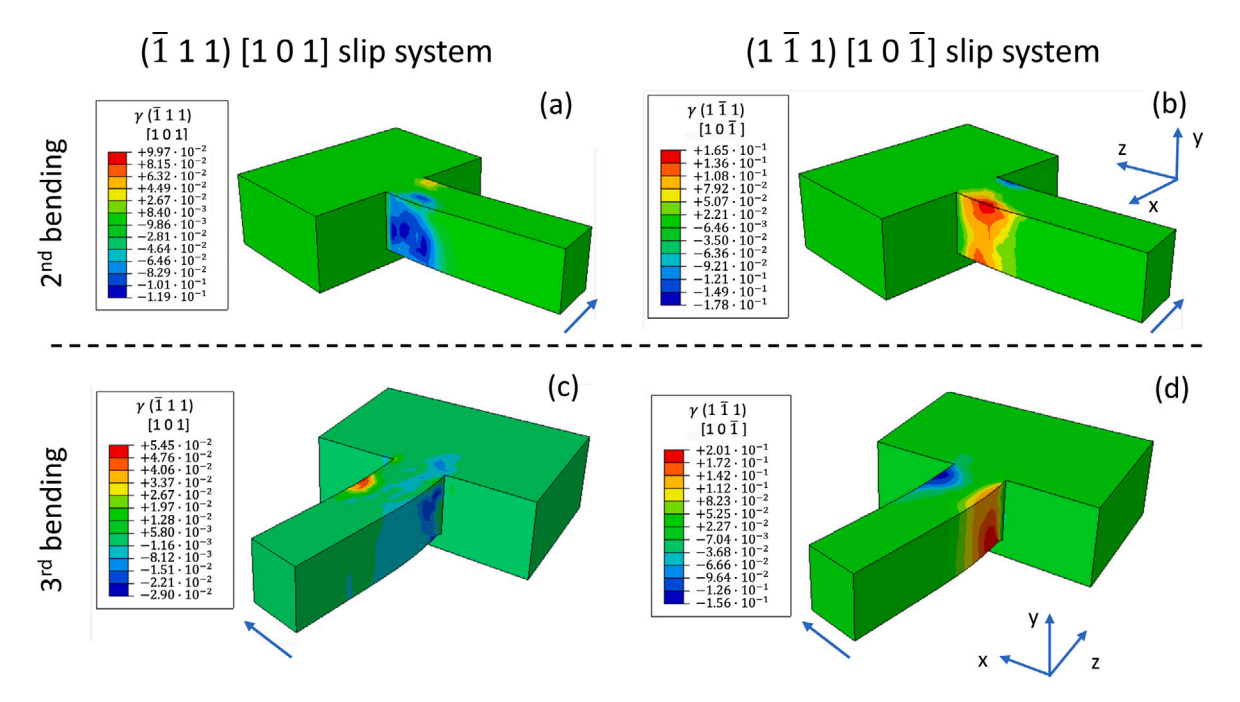


Fig. 4. (a) The slip accumulated γ in the ($\bar{1}11$)[101] slip system after 2nd bending. (b) γ in ($1\bar{1}1$)[10 $\bar{1}$] after 2nd bending. (c) γ in ($\bar{1}11$)[101] after 3rd bending. (d) γ in ($1\bar{1}1$)[10 $\bar{1}$] after 3rd bending. (For interpretation of the references to colour in this figure legend, the reader is referred to the web version of this article.)

Fig. 5 compares the force–displacement profiles of the 2nd and 3rd bending/straightening cycles of the A-F models with the experimental data. The initial A-F model (green curves), defined by Eq. (5.1) of Section 5.1, exhibits favourable agreement with the experimental (blue curves) during the bending/straightening of the 2nd cycle (Fig. 5(a, b)), but there is a notable absence of hardening during the 3rd cycle (Fig. 5(c, d)). This limitation is attributed to the saturation term A_D , which maintains the value of χ^a constant once it reaches $\chi^a = A/A_D$ (Eq. (5.1)). While the A-F model can be effective in simulating cyclic fatigue experiments, it proves inadequate for initial cycles characterized by large strains in opposite directions without saturation. This limitation is evident in our case, where there is isotropic hardening between cycles.

Similar behaviour was observed in the model proposed by *Ohno* and *Wang* (Section 5.1), which differ mainly in the curvature of the force–displacement representation (depends on the exponent "M" of the Eq. (5.3)) until it stabilizes at $\chi^a = A/A_D$ and then remains constant. A-F model without saturation ($A_D = 0$) is represented in (purple curves). The notable increase in hardening during 2rd bending

(Fig. 5(a)) results in an excessive softening of the 2rd straightening (Fig. 5(b)). Furthermore, there is no curvature in the force–displacement graph which is similar during the 2rd and 3rd cycles. This similarity between cycles demonstrates the cyclic nature of the model, which is unable to capture the increased hardening during the 3rd cycle.

The Chaboche model [41] aggregates various backstresses χ^a_k , derived from both the Armstrong-Frederick (A-F) model with and without saturation.

$$\dot{\chi}^{a} = \sum_{k=1}^{N_{B}} \dot{\chi}_{k}^{a}; \quad \dot{\chi}_{k}^{a} = A_{k} \dot{\gamma}^{a} - A_{Dk} \left| \dot{\gamma}^{a} \right| \chi_{k}^{a} \quad \text{where } A_{Dk} = 0 \text{ for some } \dot{\chi}_{k}^{a}.$$
(6.1)

The results would reflect a mixture between the green and purple curves in Fig. 5. In Fig. 5(c), the experimental force–displacement slope during the 3rd bending closely resembles that obtained during the 2nd bending. The Chaboche model is expected to exhibit a steeper slope compared to the A-F model during the 3rd bending. However, this slope would not be similar to that obtained during the 2nd bending, as certain backstresses χ^a_k become saturated during the 2nd cycle, resulting in some $\dot{\chi}^a_k=0$.

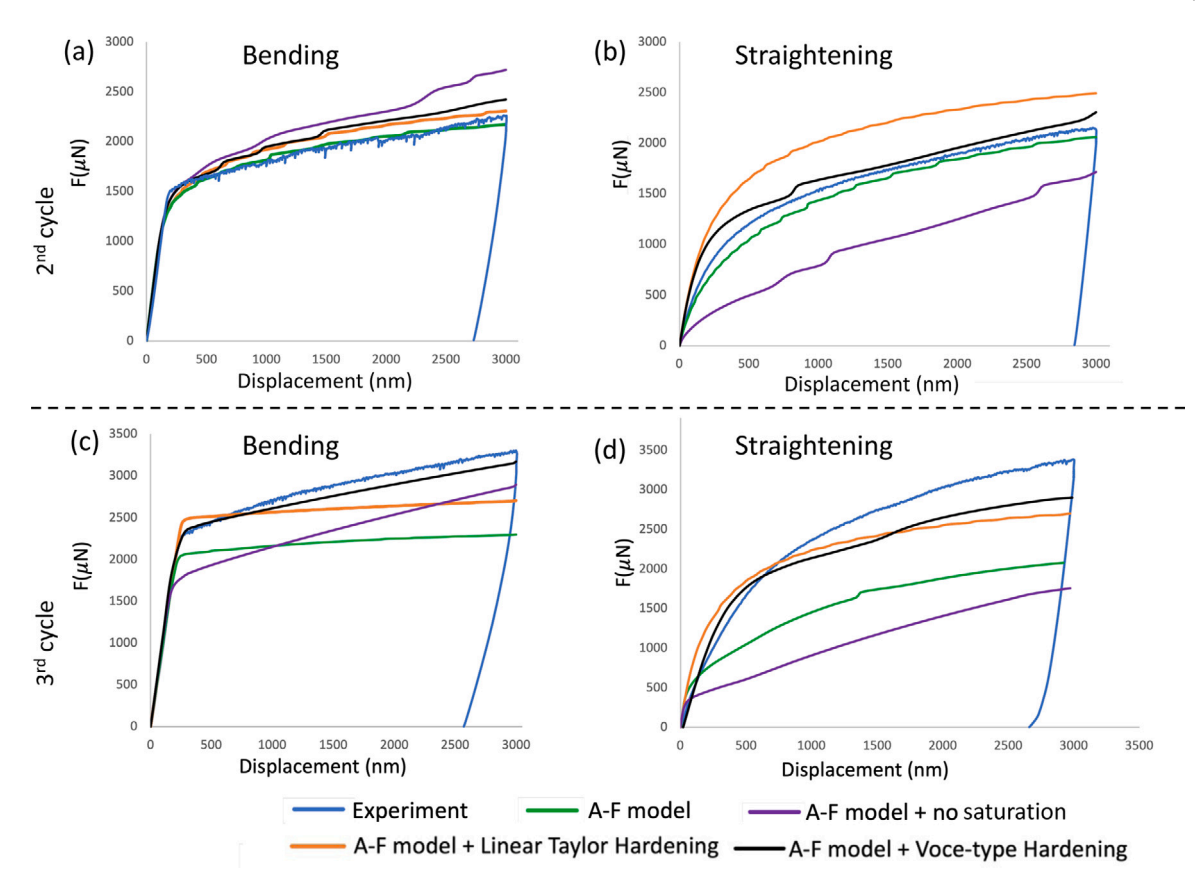


Fig. 5. Comparison of experimental data with A-F type models. (For interpretation of the references to colour in this figure legend, the reader is referred to the web version of this article.)

Another approach was to combine A-F models with Linear Taylor hardening (orange curves, Section 5.1.1). Although the 2nd bending cycle (Fig. 5(a)) demonstrates good agreement with the experimental data, a reduction of the backstress term, χ^a , was necessary during the calibration of the model to avoid excessive hardening. However, this reduction in χ^a in conjunction with linear hardening produces a higher yield strength during the 2nd straightening compared to experimental data. Furthermore, the 3rd bending cycle exhibits insufficient hardening compared to the experiment, since the linear Taylor hardening is proportional to $\sqrt{\rho^a_{SSD}} \propto \sqrt{\gamma^a}$ (see Eq. (5.4)).

With the A-F models without saturation, the same shape was observed between the 2nd and 3rd cycles (bending and straightening); however, the saturation of the force–displacement curve during straightening was less than the experimental curves, and there was no hardening between cycles. The introduction of linear Taylor hardening increases the curvature of the force–displacement curves during the straightening of the cantilever, but it does not provide enough hardening during the 3rd bending.

Finally, the A-F model was combined with *Voce-type hardening* without saturation (black curves, Section 5.1.2, Eq. (5.7)). The results agree well with the experiment, demonstrating the necessity of including isotropic hardening in A-F models.

Clarification is necessary about the saturation of the *Voce-type hardening*. Although in our parameterization there is no saturation $(A_D=0)$ in Eq. (5.1) and $\tau_c/s_s \to 0$ in Eq. (5.6)), saturation is necessary for fatigue experiments of many cycles [2,41]. The saturation is negligible for the slip, γ^a , accumulated during the first cycles (A/A_D) and s_s are much higher than the stresses reached during the experiments), but it is necessary to recalculate it once there are more cycles with more slip accumulation.

6.2. Orowan-Sleeswyk models

The GND densities of the two most active slip systems $(\bar{1}11)[101]$ and $(1\bar{1}1)[10\bar{1}]$ during the simulations are shown in Fig. 6. They were calculated by solving the Nye tensor in its matrix form (see Section 4), the results show the highest concentration in the base of the cantilever, since it is the region where the curvature is the highest.

During the 2nd bending, it can be observed how a slip band of positive GND is formed in both slip systems (see Fig. 6(a, b)). Applying the formulation of Dai et al. [51] for small strains, we can check the sign of the edge GND using an analytical expression.

$$\varrho_{GND,e}^a = -\frac{1}{b^a} \nabla \gamma^a \cdot s^a. \tag{6.2}$$

For $(\bar{1}\ 1\ 1)[1\ 0\ 1]$, the direction of $\nabla \gamma^a$ is along -x (see Fig. 4(a)) that corresponds to $[\bar{5}\ \bar{2}\ \bar{2}1]$ in the crystal system for the Euler angles $\phi_1=260.0^\circ,\ \Phi=101.1^\circ$ and $\phi_2=248.2^\circ$ [19]:

$$sign(\rho_{GND,e}^{a}) = -\nabla \gamma^{a} \cdot s^{a} = -[\bar{5} \ \bar{2} \ \bar{21}] \cdot [1 \ 0 \ 1] = +$$
(6.3)

For $(1\ \bar{1}\ 1)[1\ 0\ \bar{1}]$, the direction of $\nabla \gamma^a$ is +x (see Fig. 4(a, b)) that corresponds to [5 2 21]:

$$\mathrm{sign}(\varrho_{GND,e}^{a}) = -\nabla \gamma^{a} \cdot s^{a} = -[5 \ 2 \ 21] \cdot [1 \ 0 \ \bar{1}] = + \tag{6.4}$$

The same procedure can be used for the sign of GND during the 3rd bending, in this case, $\rho_{GND} < 0$.

Fig. 6 shows a high concentration of GND at the base of the cantilever during the 2nd and 3rd bending cycles, reaching densities of $\sim \pm 130~\mu m^{-2}$ for ($\bar{1}~1~1)[1~0~1]$ and $\sim \pm 160~\mu m^{-2}$ for ($\bar{1}~\bar{1}~1)[1~0~\bar{1}]$. The maximum total value of GND (the sum of all GND) is $\sim |10^3|~\mu m^{-2}$, a value of the same order of magnitude as the values obtained through KAM images [19]. During 2nd and 3rd straightening, the GND density was very low. This happens because the GND is calculated from the

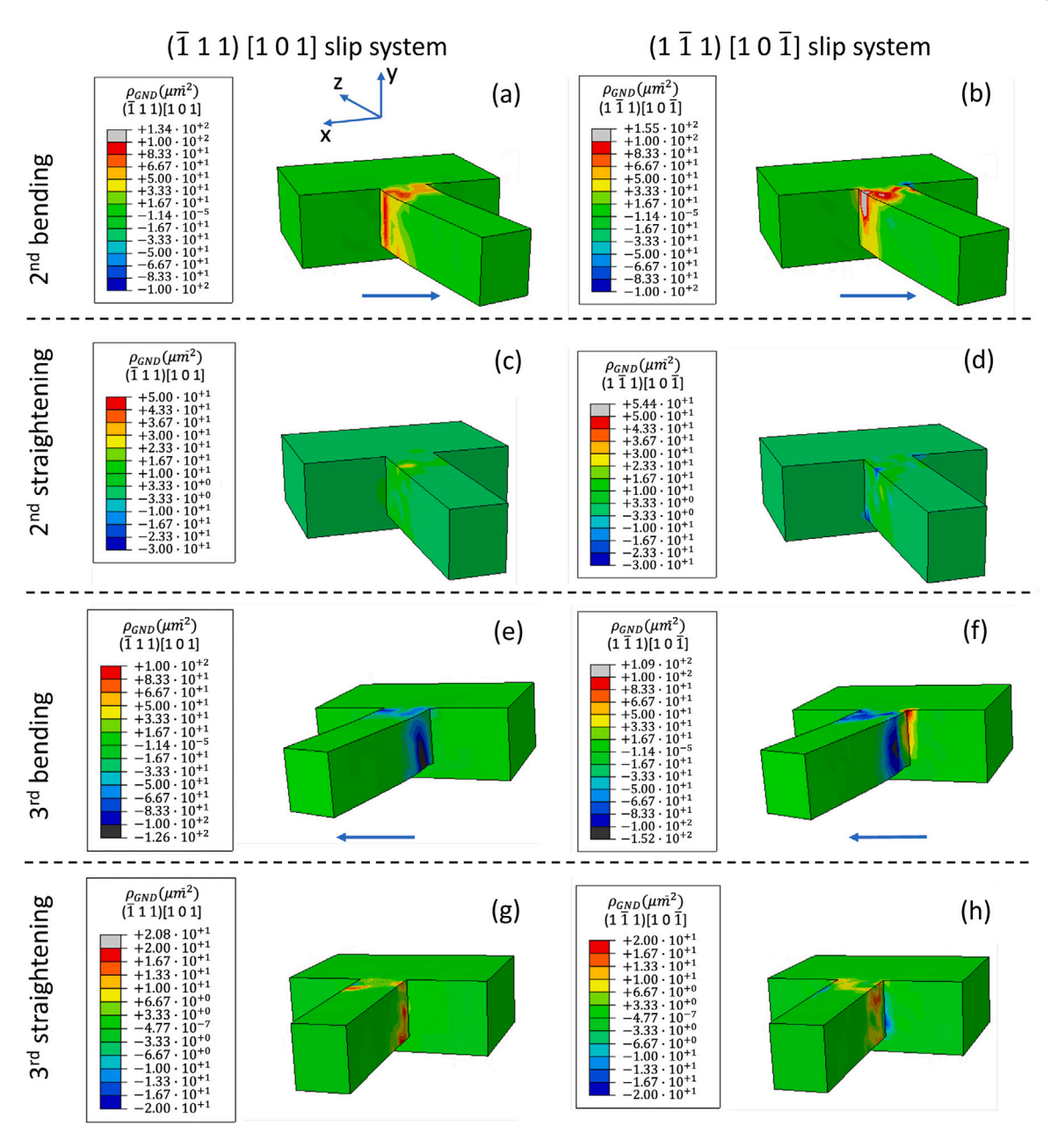


Fig. 6. Edge GND profiles of the two more active slip systems (\bar{l} 1 1)[1 0 1] and (1 \bar{l} 1)[1 0 \bar{l}] after the 2nd and 3rd cycles. Please, be aware that the colour scale is adjusted in the straightening figures (c,d,g,h) where the GND density is significantly smaller and difficult to appreciate the distribution with the bending colour scale. (For interpretation of the references to colour in this figure legend, the reader is referred to the web version of this article.)

plastic strain gradient, \boldsymbol{F}_p , and when the cantilever returns to its original position, the strain disappears.

Fig. 7 shows the force–displacement curves for the Orowan-Sleewyck model with and without SSD modification during the 2nd and 3rd cycles of the experiment.

The golden curve represents the force–displacement obtained from the Orowan-Sleeswyk model. There is a good match with the experimental data during the 2nd bending Fig. 7(a) presenting slightly low yield stress but reaching the maximum force measured experimentally. However, during the 2nd straightening (Fig. 7(b)), we observed a lower strain hardening than experiments and the maximum force reached is approximately the initial yield value presented in curve Fig. 7(a), which is expected since this force occurs when the beam is straight and $\rho_{GND}\sim0~\mu\text{m}^{-2}.$

The 3rd cycle is shown in Fig. 7(c) (bending) and Fig. 7(d) (straightening), the shape of the curve is similar to the 2nd cycle with slightly

more hardening during bending and more backstress during straightening, these shapes are reasonable since the deformation is similar but in opposite direction. The slightly higher hardening can be attributed to the GND that remain in the corners after the previous cycle.

Table 6.2 includes the parameters that have been adjusted using the Nelder–Mead optimization algorithm (Section 5.3). The *Orowan-Sleeswyk* models were calibrated with a geometrical factor $C_d=3.6$ (Eq. (5.8)). For comparison, the value reported by Sleeswyk with a low carbon steel alloy [10,52] was $C_d\sim10$. In both cases the material was FCC and there were bands (slip for copper and Lüdder for steel) with $\rho_{GND}\sim10^3~\mu\text{m}^2$ around them. Nevertheless, the model seems incomplete when we compare straightening curves with the experiment, which presents an excessive hardening no explained for the Orowan-Sleeswyk formula (Eq. (5.8)).

We examined the possibility that dislocations do not disappear during straightening. Ugi et al. [20] did HR-ESBD measurements of the

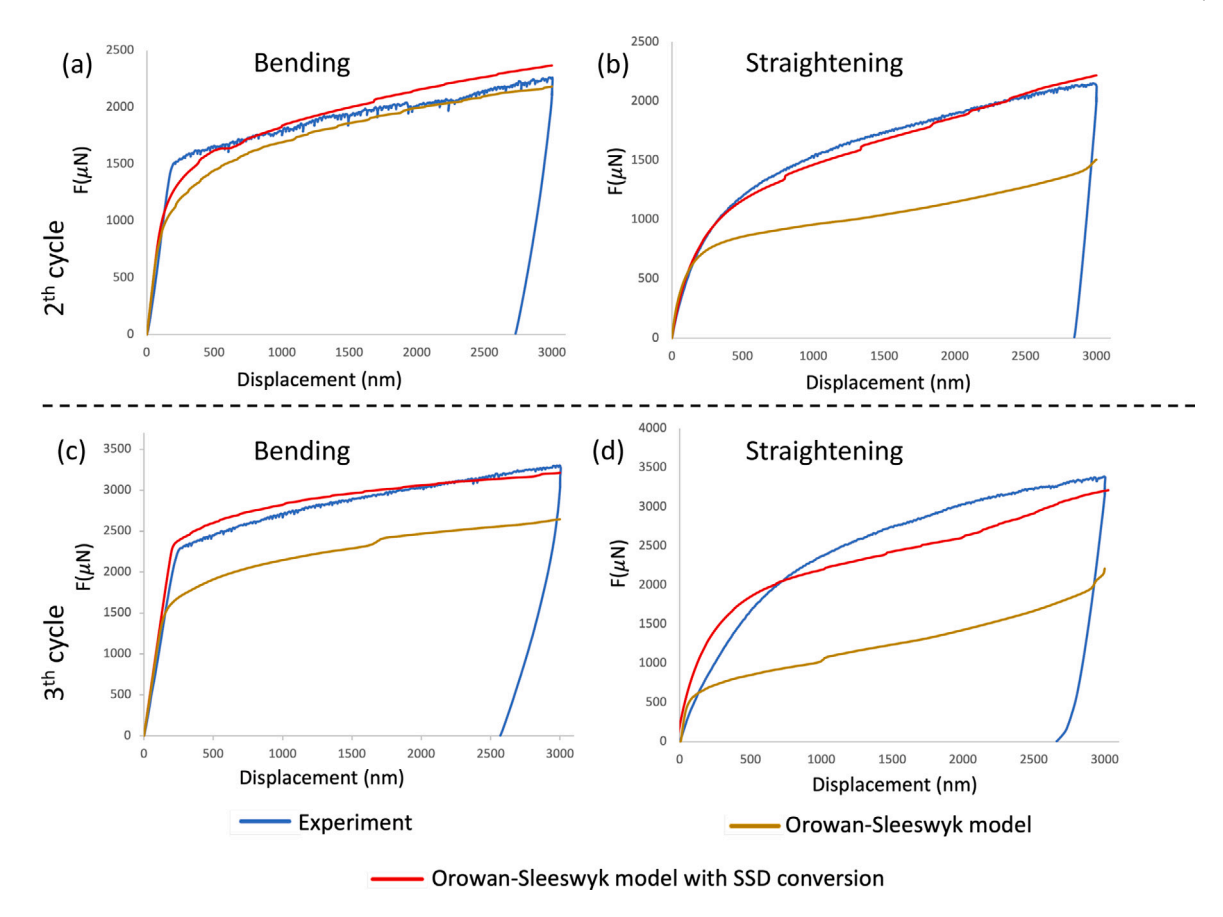


Fig. 7. Comparison of experimental data with Orowan-Sleeswyck model and Orowan-Sleeswyck with SSD conversion. (For interpretation of the references to colour in this figure legend, the reader is referred to the web version of this article.)

monocrystal copper cantilever, and they observed that during straightening some GND changed their orientation, forming complex structures whose contribution to strain hardening ${\sim}0$ (because dislocations do not have a clear orientation). In general, only ${\sim}25\%$ GND were recombined instead of total recombination, as shown by the Orowan-Sleeswyk model combined with the GND calculus model (see Section 4).

GND model	Parameters adjusted
Orowan-Sleeswyk (Eq. (5.8)) Orowan-Sleeswyk (Eq. (5.8)) with SSD	$C_d = 3.6$ $C_d = 3.6$ and $\lambda = 0.72$
(Eq. (5.10))	od sto did n on 2

Orowan-Sleeswyk model with SSD (red curves) includes a representation of the previously mentioned complex dislocation structures. As discussed in Section 5.2.1, we approximate these structures as increase in the SSD density, giving a random orientation to these GND when they change. The hardening produced by the SSD increment is given by Taylor equation (Eq. (5.4)). The percentage of GND density converted to SSD density during straightening was adjusted to 72% (parameter λ), a value close to the ~75% GND that remain after straightening in the experiment described in [20].

The force–displacement profile shows good agreement with the experimental data (Fig. 7) that reproduce the hardening expected during straightening. The highest mismatch is presented in the 3rd straightening, where the experimental slope is lower than the rest of the straightening cases; the reason that we found most probable comes from the indentation process, which is not perfectly perpendicular after 3 consecutive cycles and requires an adaptation of the cantilever to the indenter shape, reducing the stiffness of the structure.

6.3. Modelling bending/straightening 1st cycle

Once the parameterization of the models was adjusted for the 2nd and 3nd cycles, where slip bands are completely formed, they were applied to the 1st cycle to estimate the impact associated with the slip band formation process. The models and parameters applied were those that have proven capable of reproducing the Bauschinger effect during initial cycles: A-F combined with Voce-type model and "modified" Orowan-Sleeswyk model by SSD density conversion. For modelling the 1st cycle only the parameter CRSS was changed to 30 MPa, which differs from the 43 MPa of the 2nd cycle. The increase in the 2nd cycle is due to the hardening during the 1st cycle.

Fig. 8(a) presents the force–displacement results from the 1st bending. Experiment results show less hardening (\sim 540 µN) than simulations (\sim 950 µN for Orowan-Sleeswyk + SSD conversion and \sim 1100 µN for A-F+Voce). The experimental curve also exhibits several drops or discontinuities, with the largest drop \sim 1000 µN. These drops, attributed to slip bands formation (see Fig. 1b), appear responsible for the different stress–strain experimental response in 1st cycle compared to the 2nd and 3rd. Confirming this hypothesis, our simulations, which do not include the slip bands effect, show similar hardening in the 1st, 2nd and 3rd cycles. Once formed, the slip bands act as obstacles to dislocations [12], increasing the hardening of posterior cycles.

Fig. 8(b) presents the force–displacement results from the straightening process. The absence of drops indicates that the slip bands formation mainly occurs during the bending of 1st cycle. These results discard the hypothesis that the force drops are due to cantilever adaptation to the indenter, as the cantilever must also adapt during the 1st straightening to the indenter on the opposite beam face. The experimental data and simulations show good agreement.

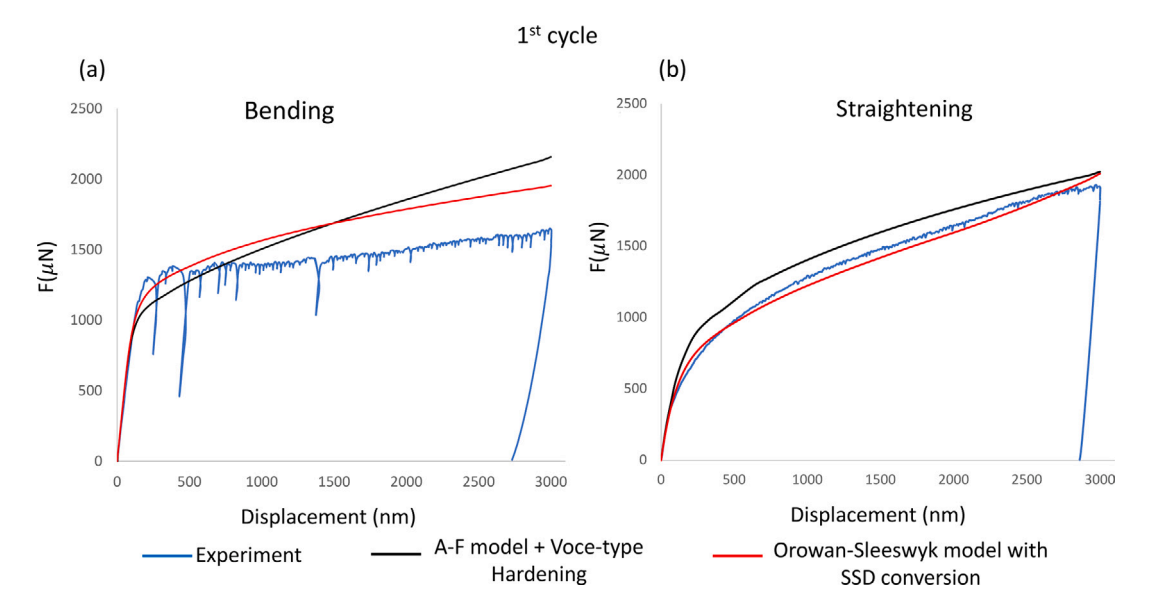


Fig. 8. Comparison of 1st cycle experimental data with "modified" Orowan-Sleeswyck with SSD conversion and A-F model with Voce type hardening.

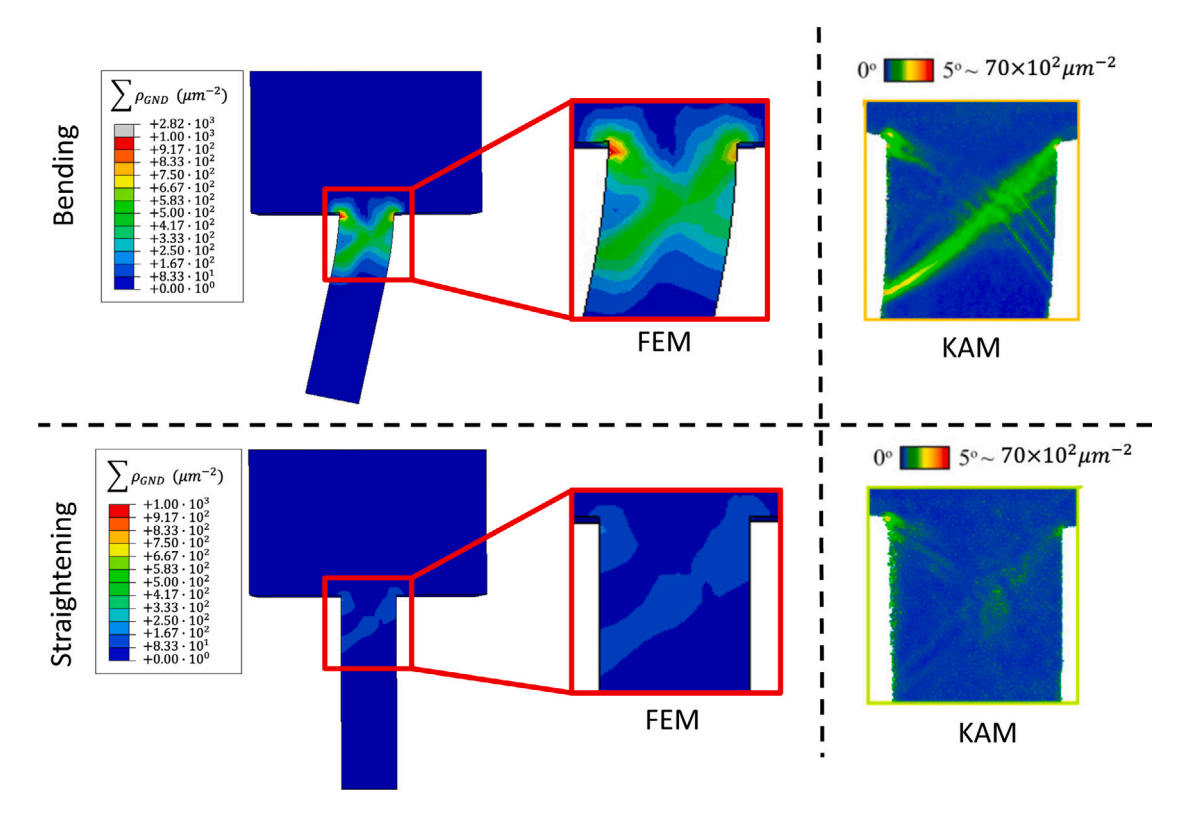


Fig. 9. Comparison of maps of total GND density between simulations and experimental estimations using KAM analysis based on three nearest neighbours [46] after the 1st cycle.

The effect of slip bands on total GND distribution is analysed by comparing simulated GND density (Fig. 9) with experimental estimations from kernel average misorientation (KAM) analysis [46]. KAM data was calculated from the misorientation gradient of each EBSD data point of the Cu cantilever relative to its first, second and third nearest neighbour points. It measures local lattice curvature, and thus, GND density. The calculation of the GND density from the lattice curvature, as described in [53], uses elastic rotation gradients to determine the incompatibility of the lattice (valid only for small deformations [54]), employing L1 minimization to identify 9 unknown GND densities that accommodate a given lattice curvature. In contrast, our model uses the

plastic deformation gradient F_p and a restricted solution for 18 possible GND densities described in [22].

Fig. 9 shows an "X-shape" GND distribution in both simulations and KAM analysis. The simulations exhibit a more uniform distribution across the cantilever, while the KAM analysis reveals higher concentrations within the slip bands. During straightening, both simulations and KAM analysis show a significant reduction in GND density at the cantilever's corners and edges. The KAM image shows high GND concentrations due to the slip bands but it is noteworthy that the KAM analysis is designed for small strains.

Although slip bands were not directly simulated, the model reproduces a very similar GND distribution, suggesting it represents a state preceding the abrupt slips observed believing it could be obtained experimentally using a lower strain rate. While the geometric effect of the slip bands in Eqs. (5.8) and (5.10) is evident, the current lack of activation of dislocation sources [49] prevents separating this effect from the constants C_d and λ .

We conclude that our models still have room for improvement. It represents a step towards creating shape and size-independent models (due to the use of GND), but requires considering dislocation sources to model and predict GND concentration.

6.4. Comparison of A-F model with Voce-type hardening and Orowan-Sleeswyk model with SSD

The force–displacement profiles of both models demonstrate that the two alternatives are able to reproduce the Bauschinger effect during initial cycles (Figs. 5, 7).

The *Orowan-Sleeswyk* model with SSD conversion introduces the physical concept of dislocations such as GND and SSD and their evolution. These models allow us to better understand the internal processes in the material for more complex experiments or other materials. On the other hand, the *A-F with Voce-type hardening* is based on a mathematical approach that considers the relationships between stress, slip γ , and different parameters that need adjustment.

The *Orowan-Sleeswyk* model requires solving Nye's dislocation tensor, making it computationally more complex and prone to convergence issues (especially at the corners), while the *A-F* model performs better for coarser meshes and is more practical if the goal is to model material fatigue over multiple cycles.

Numerous studies have corroborated that hardening saturates after several cycles or higher strains [2,41]. In the initial cycles, there was no saturation, so adjustment of the saturation parameters in the A-F model with Voce-type hardening was not necessary ($A_D \sim 0$ in Eq. (5.1) and $\tau_c/s_s \sim 0$ in Eq. (5.6)). However, when the models are used in a cyclic regimen, the A-F with Voce-type hardening requires calibration of four parameters. In contrast, the modified Orowan-Sleeswyk model does not need additional parameters since the hardening and Bauschinger effect are proportional to $\sqrt{\rho_{GND}}$, attenuating the slope for higher values of ρ_{GND} .

6.5. Improvement to the Orowan-Sleeswyk model with SSD after multiple cycles

We propose enhancements to the *Orowan-Sleeswyk* model with SSD conversion, incorporating strain rate influence, slip bands effects and cracking due to fatigue accumulation. These enhancements are derived from a literature review and require validation through additional multi-cycle cantilever experiments.

• Strain rate influence: Comparing the experiments of the data used in Demir et al. [19] and Ugi et al. [20], the load rate was different. In Demir et al. the load rate was 1 $\mu m\ s^{-1}$ for a 25.4 \times 8.64 \times 7.05 μm cantilever, while in Ugi et al. the load rate was 5 nm s^{-1} for a 20.6 \times 5.0 \times 5.0 μm cantilever. The difference in the strain rate might be responsible for less isotropic hardening during the straightening in Ugi et al. since there is more time for the dislocations to recombine.

However, this lower strain rate also led to fewer slip band formations in the Ugi et al. cantilever, occurring only at the cantilever's corner. Slip bands play an important role as dislocation obstacles increasing the strain hardening during the initial cycles but also in dislocation recombination by reducing hardening after multiple cycles (reaching dislocation density saturation) and initiating fatigue cracks, as shown in [55,56].

The SSD conversion mechanism (Eq. (5.10)) should be positively correlated with the strain rate, however, it also should be positively correlated with any dislocation saturation term derived from slip band formation.

• Slip Bands effects: Essmann et al. [57] identified slip bands in single-crystal copper during uniaxial loading fatigue experiments and subsequently proposed the EGM model [55] to explain the slip bands formation, dislocation recombination, and crack development over multiple loading cycles. The formation of slip bands is attributed to the interaction between strain with material extrusions and intrusions. During the initial loading cycles, the dislocation structure exhibits a disorganized pattern, resulting in an accumulation of dislocations over consecutive cycles. This process reaches saturation after approximately 50 cycles, in which steady-state cyclic deformation is established due to dislocation recombination within the slip bands, achieving a balance between dislocation multiplication and recombination [58].

During steady-state, dislocations form intricate clusters called "veins" outside the slip bands, similar to structures observed in the early cycles. Within the slip bands, edge dislocation density varies, forming high-density and low-density areas known as "cells". The cell characteristics may differ in cantilevers compared to uniaxial loading experiments due to curvature effects, which create distinct tensile and compressive regions separated by a neutral axis.

Modelling dislocation recombination through slip bands can be achieved by incorporating an attenuation term inside Eq. (5.10). However, accurate local strain prediction after multiple cycles requires modelling slip bands, including both dislocation sources (extrusions and intrusions) [49] and the recombination mechanisms that occur inside the slip bands [59].

• Cracking due to fatigue accumulation: Strain accumulation within slip bands leads to crack initiation when edge dislocations from separate slip systems recombine. The extrusions or intrusions must be left over debilitating the structure [58]. Cracks can form at the interface between slip bands and the surrounding material or in the rugosity that is formed in the surface of the material due to slip bands [55]. In polycrystals, cracks might also occur at crystal interfaces [60]. In cantilevers, the neutral axis of curvature acts as a dislocation barrier, potentially functioning similar to polycrystal interfaces.

In summary, understanding strain rate effects on fatigue accumulation, slip bands and crack formation is crucial for enhancing the *Orowan-Sleeswyk* model with SSD conversion. The literature shows that loading rate variations affect slip band formation and dislocation behaviour, which are crucial for crack development. Additional cantilever experiments with extended cycles are needed to validate these proposed improvements and expand our understanding of dislocation processes.

7. Conclusions

In this study, we applied well-established models in cyclic deformations to reproduce the Bauschinger effect observed in a copper monocrystal cantilever experiment during the initial bending and straightening cycles. These models were implemented with the UKAEA's Crystal Plasticity Finite Element code (OXFORD-UMAT); UMAT files, documentation, and examples are available in the GitHub link with open public access [24]. The principal findings are as follows.

• The Armstrong-Frederick model and their variants (Chaboche, Ohno and Wang) failed to replicate the experimental data. The parameters necessary to attenuate the straightening phase result in excessive saturation during subsequent cantilever bending, reaching a point where the resistance no longer increases. While these models are very useful for understanding multiple deformation cycles, they are not suitable for reproducing the initial cycles.

- The combination of Armstrong-Frederick and Voce-type hardening models has proven effective in simulating the initial cycles. The results reveal the confluence of two forms of hardening: the reversible type represented by the Armstrong-Frederick model, which arises during bending and contributes to the Bauschinger effect, and the irreversible type represented by the Voce-type hardening model.
- The *Orowan-Sleeswyk* model failed to replicate the experimental data. Although the hardening is appropriate during the bending, the values obtained during the straightening are well below the experimental results. This discrepancy can be attributed to the near-zero density of geometrically necessary dislocations (GND) when the cantilever is straight, as per the GND formulation.
- In this study we propose to enhance the *Orowan-Sleeswyk* model by integrating the conversion of certain GND into statistically stored dislocations (SSD). This alternative has proven to be effective in simulating the initial cycles. According to recent research suggesting that a percentage of GND do not recombine during the straightening phase, but rather reorient, leading to increased hardening, our innovation involves considering that a percentage of the GND density reduced is converted to SSD density and incorporating it into the model.
- Both models: Armstrong-Frederick with Voce-type hardening and Orowan-Sleeswyk with SSD are valid alternatives with similar accuracy to reproduce the hardening and Bauschinger effect during the initial cycles. Some of the most significant differences in the choice of one or the other are: Orowan-Sleeswyk with SSD allows us to better understand the internal physical mechanisms of the material and is easier to adjust because there are no saturation parameters as the kinematic hardening is proportional to the square root of the GND density, however, it is more computationally complex and prone to convergence issues. On the other hand, Armstrong-Frederick and Voce-type hardening works better with coarser meshes but it is complicated to adjust several saturation parameters that vary after several cycles or big strains.
- Future research derived from this study should focus on two main areas: Studying how slip bands formation affects the hardening and Bauschinger effect across initial and posterior cycles, and investigating the impact of GND and SSD in polycrystalline materials. Additional cantilever experiments with extended cycles will be necessary to validate and expand our understanding of dislocation dynamics.

CRediT authorship contribution statement

Alvaro Martinez-Pechero: Writing – review & editing, Writing – original draft, Visualization, Validation, Software, Resources, Methodology, Investigation, Formal analysis, Data curation, Conceptualization. Eralp Demir: Writing – review & editing, Supervision, Software, Formal analysis, Conceptualization. Chris Hardie: Writing – review & editing, Supervision, Funding acquisition. Yevhen Zayachuk: Writing – review & editing, Supervision, Funding acquisition. Anna Widdowson: Writing – review & editing, Supervision, Funding acquisition. Edmund Tarleton: Writing – review & editing, Supervision, Project administration, Funding acquisition.

Declaration of competing interest

The authors declare that they have no known competing financial interests or personal relationships that could have appeared to influence the work reported in this paper.

Acknowledgements

The authors acknowledge Vikram Phalke from UKAEA for the useful discussions about copper CP law. This work has been part-funded by the EPSRC Energy Programme, UK [grant number EP/W006839/1]. E. Tarleton acknowledges financial support from the Royal Academy of Engineering through a Senior Research Fellowship, UK. For the purpose of open access, the author(s) has applied a Creative Commons Attribution (CC BY) licence (where permitted by UKRI, 'Open Government Licence' or 'Creative Commons Attribution No-derivatives (CC BY-ND) licence' may be stated instead) to any Author Accepted Manuscript version arising.

Appendix A. Crystal to sample transformation

Crystal to sample transformation, g, defines the passive transformation from the crystal to the sample reference frame (see Eq. (A.1) which is given in Box I). g is computed by the Bunge angles ($\varphi_1, \Phi, \varphi_2$).

Appendix B. Rotation matrix for elastic constants

The transformation of the elastic matrix in the crystal reference \mathbb{C}_0 into the elasticity matrix in the deformed configuration \mathbb{C} is given by $\mathbb{C} = [R] [\mathbb{C}_0] [R]^T$.

[*R*] a 6 × 6 special transformation matrix 6 × 6 constructed from the crystal to the sample transformation matrix (g_{ij}) [34] (see Eq. (B.1) which is given in Box II).

Appendix C. Convergence study

Fig. C.1 illustrates the convergence study of the cycles for different mesh sizes:

Appendix D. Slip systems activation

The activation of the slip systems depends on the Schmid factor m and CRSS. The Schmid factor (m) for a stress σ is given by the product $m=(\sigma\cdot s^a)\cdot (\sigma\cdot n^a)/(|\sigma\cdot s^a|\cdot |\sigma\cdot s^a|)$, where n^a and s^a are the normal and slip direction of the slip system, respectively. The calculation of the Schmid factor for the main stress component σ_z in the cantilever experiment (see Fig. 3(b)) is presented in Table D.1:

The Schmid factor is higher in slip systems (1 $\bar{1}$ 1) [1 0 $\bar{1}$] and ($\bar{1}$ 1 1) [1 0 1]. In Fig. D.1, we can observe the amount of slip after applying the second bending. We can see how γ decreases in subsequent slip systems, being almost imperceptible compared to the two main ones. The explanation for this occurrence is that the plasticity generated by the slip of (1 $\bar{1}$ 1) [1 0 $\bar{1}$] and ($\bar{1}$ 1 1) [1 0 1] induces stress relaxation, preventing the activation of subsequent slip systems. For this reason, we focus our analysis of slip and dislocations only on the first two (see Figs. 4 and 6).

Table D.1 Schmid factors of slip systems respect to $\sigma_z = [\bar{5}, 2, 1]$.

Slip normal	Slip direction	Schmid factor respect to $\sigma_z = [\bar{5}, 2, 1]$
1, Ī, 1)	[1,0,1]	0.49
$[\bar{1}, 1, 1)$	[1, 0, 1]	-0.43
$(1, 1, \bar{1})$	$[1, \bar{1}, 0]$	0.38
$(\bar{1}, 1, 1)$	[1, 1, 0]	-0.32
$[1, \bar{1}, 1)$	[1, 1, 0]	0.24
$1, \bar{1}, 1)$	[0, 1, 1]	-0.24
$1, 1, \bar{1})$	[1, 0, 1]	-0.21
(1, 1, 1)	$[1, \bar{1}, 0]$	-0.19
(1, 1, 1)	$[1, 0, \bar{1}]$	0.16
$(1, 1, \bar{1})$	[0, 1, 1]	-0.16
$\bar{1}, 1, 1)$	$[0, 1, \bar{1}]$	0.1
[1, 1, 1)	$[0, 1, \bar{1}]$	-0.02

$$\mathbf{g} = \begin{bmatrix} \cos \varphi_1 \cos \varphi_2 - \sin \varphi_1 \sin \varphi_2 \cos \boldsymbol{\Phi} & \sin \varphi_1 \cos \varphi_2 - \cos \varphi_1 \sin \varphi_2 \cos \boldsymbol{\Phi} & \sin \varphi_2 \sin \boldsymbol{\Phi} \\ -\cos \varphi_1 \sin \varphi_2 - \sin \varphi_1 \cos \varphi_2 \cos \boldsymbol{\Phi} & -\sin \varphi_1 \sin \varphi_2 + \cos \varphi_1 \cos \varphi_2 \cos \boldsymbol{\Phi} & \cos \varphi_2 \sin \boldsymbol{\Phi} \\ \sin \varphi_1 \sin \boldsymbol{\Phi} & -\cos \varphi_1 \sin \boldsymbol{\Phi} & \cos \boldsymbol{\Phi} \end{bmatrix}^T.$$
(A.1)

Box I.

$$[\mathbf{R}] = \begin{bmatrix} (g_{11})^2 & (g_{12})^2 & (g_{13})^2 & 2 g_{11} g_{12} & 2 g_{13} g_{11} & 2 g_{12} g_{13} \\ (g_{21})^2 & (g_{22})^2 & (g_{23})^2 & 2 g_{21} g_{22} & 2 g_{23} g_{21} & 2 g_{22} g_{23} \\ (g_{31})^2 & (g_{32})^2 & (g_{33})^2 & 2 g_{31} g_{32} & 2 g_{33} g_{31} & 2 g_{32} g_{33} \\ g_{11} g_{21} & g_{12} g_{22} & g_{13} g_{23} & g_{11} g_{22} + g_{12} g_{21} & g_{13} g_{21} + g_{11} g_{23} & g_{12} g_{23} + g_{13} g_{22} \\ g_{31} g_{11} & g_{32} g_{12} & g_{33} g_{13} & g_{11} g_{22} + g_{12} g_{21} & g_{13} g_{21} + g_{11} g_{23} & g_{12} g_{23} + g_{13} g_{22} \\ g_{31} g_{11} & g_{32} g_{12} & g_{33} g_{13} & g_{11} g_{32} + g_{12} g_{31} & g_{13} g_{31} + g_{11} g_{33} & g_{12} g_{33} + g_{13} g_{32} \\ g_{21} g_{31} & g_{22} g_{32} & g_{23} g_{33} & g_{22} g_{31} + g_{21} g_{32} & g_{21} g_{33} + g_{23} g_{31} & g_{22} g_{33} + g_{23} g_{32} \end{bmatrix} .$$

Box II.

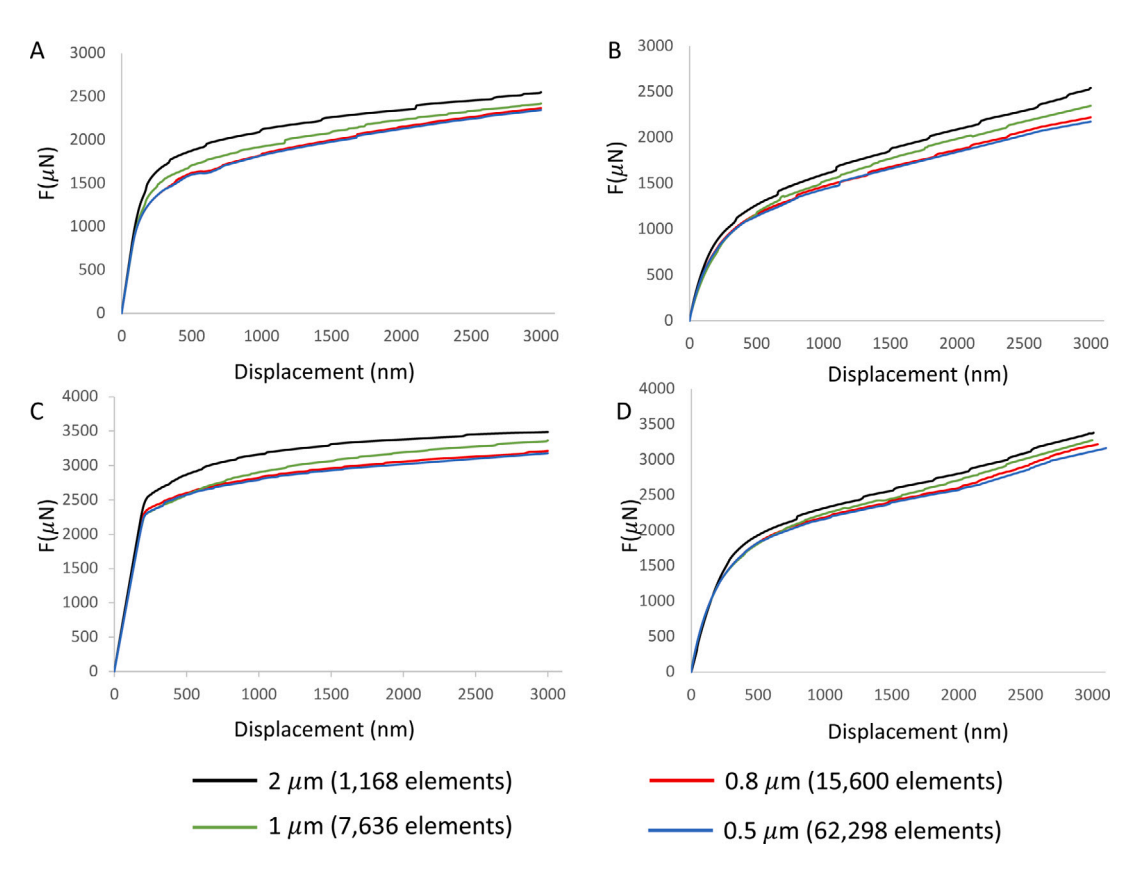


Fig. C.1. Convergence study for 2nd and 3rd cycles.

Appendix E. Comparison of Node Line and indenter

In this section, we analyse if incorporating the indenter into the model significantly alters the results compared to a line of element nodes (Node Line) as a substitute for the indenter. Modelling the indenter provides a more accurate representation of the contact mechanics, including stress distributions and potential deformation of both the indenter and the material being tested. However, Demir et al. [19] determined that the volume affected by the indenter contact is very small (2 μm^3) compared to the deformed volume of the cantilever (180 μm^3), suggesting that its effect can be neglected.

In our models, the indenter was represented with a spherical tip of approximately 5 μm of radius. In Abaqus, the contact was modelled with "hard normal" and "rough friction". Fig. E.1 compares the

force–displacement responses of modelling the indenter and using the Node Line representation. The results demonstrate minimal differences between the two loading methods.

The spherical indenter exhibited slightly higher resistance, potentially due to its contact point of 1.5 μm of radius. This contact point generates less torque and promotes greater force dissipation in the contact area compared to the distributed load of the Node Line, thus requiring more force to achieve equivalent displacement.

Fig. E.2 presents the stress profiles of the indenter and the Node Line. The continuous Node Line applies a distributed load, which creates a larger moment arm relative to the cantilever's fixed end. In contrast, the spherical indenter applies a concentrated force, resulting in a smaller effective lever arm. This localized pressure in the contact region induces higher local stress concentrations, as evidenced by peak

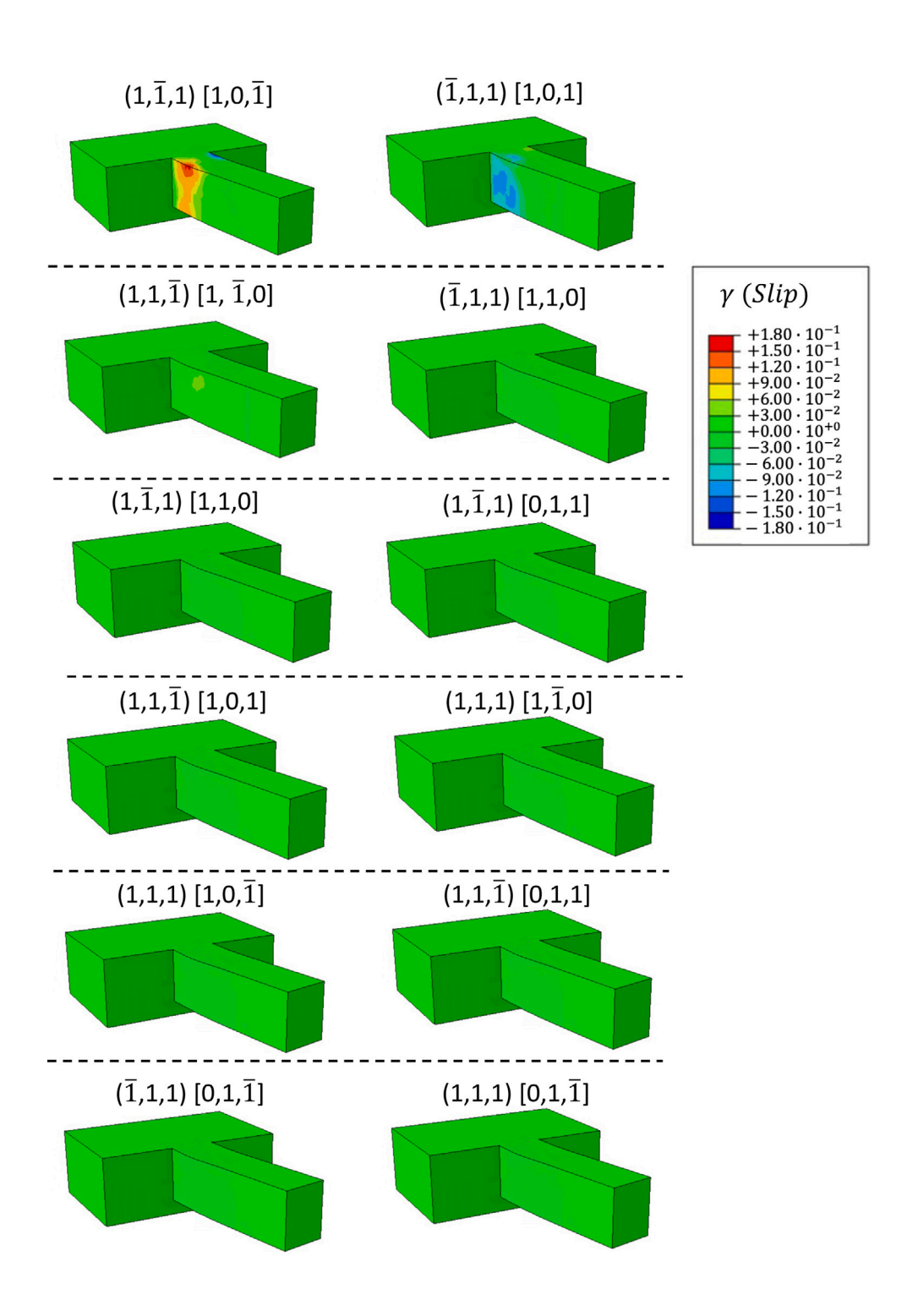


Fig. D.1. Accumulated slip γ after the 2nd bending of all the slip systems.

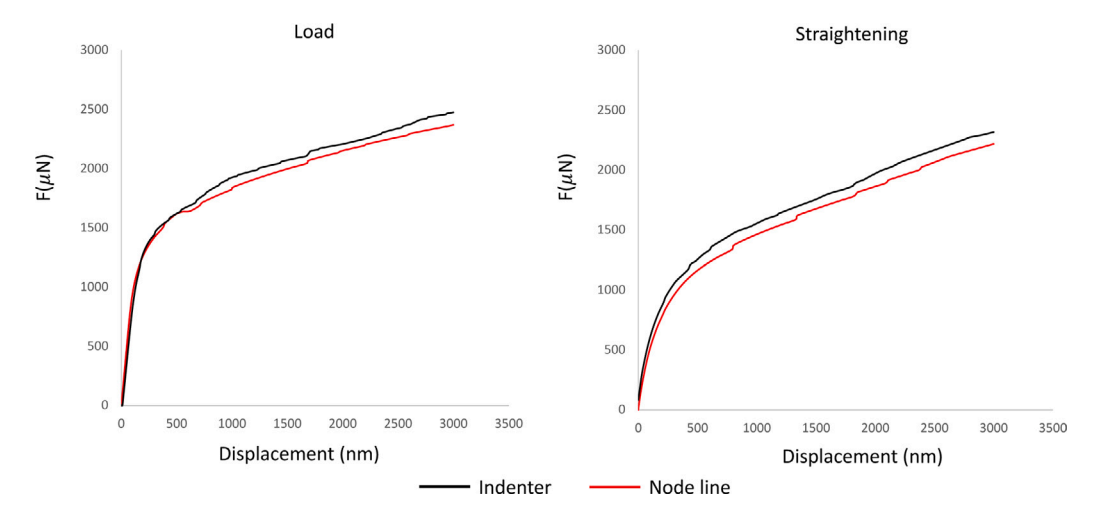


Fig. E.1. Comparison of force-displacement response using a line of nodes or an indenter during the 2nd cycle. (For interpretation of the references to colour in this figure legend, the reader is referred to the web version of this article.)

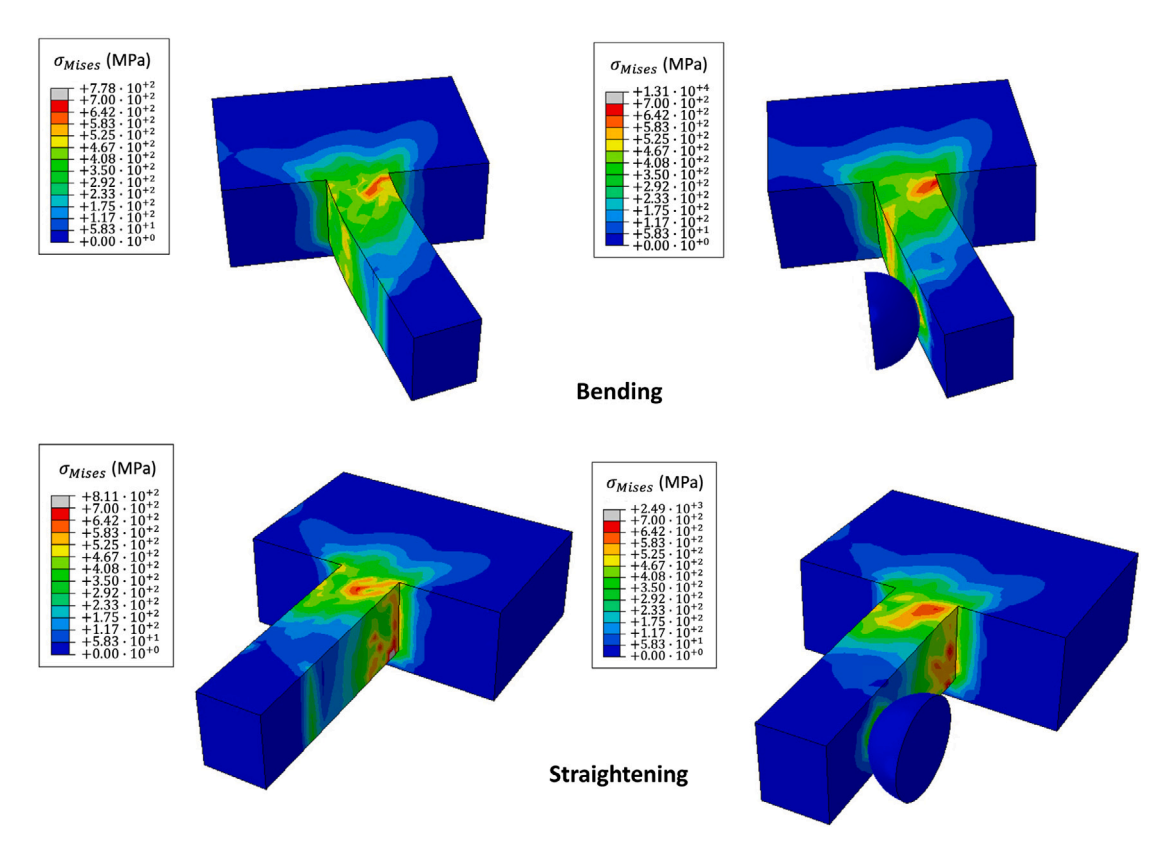


Fig. E.2. Stress profile of the cantilever after the 2nd cycle with Node Line (left) and Indenter (right).

stress values that are nearly two orders of magnitude compared to those observed in the Node Line simulations (as indicated by the maximum values on the colour gradient scale in Fig. E.2).

Using an indenter instead of a Node Line causes convergence issues in simulations when the indenter detaches from the sample, typically occurring between cycles. This may be due to the "rough friction" contact, which may not effectively handle the sliding of the indenter during unloading. As a result, the Node Line is a more practical approach for modelling the cycles with a reduced loss of precision.

References

[1] M. Lipa, A. Durocher, R. Tivey, T. Huber, B. Schedler, J. Weigert, The use of copper alloy CuCrZr as a structural material for actively cooled plasma facing

- and in vessel components, Fusion Eng. Des. 75 (2005) 469-473.
- [2] J.-H. You, M. Miskiewicz, Material parameters of copper and CuCrZr alloy for cyclic plasticity at elevated temperatures, J. Nucl. Mater. 373 (1–3) (2008) 269–274.
- [3] X. Hu, C. Wei, H. Margolin, S. Nourbakhsh, The Bauschinger effect and the stresses in a strained single crystal, Scr. Met. Mater. 27 (7) (1992) 865–870.
- [4] L.E. Levine, M.R. Stoudt, A. Creuziger, T.Q. Phan, R. Xu, M.E. Kassner, Basis for the Bauschinger effect in copper single crystals: changes in the long-range internal stress with reverse deformation, J. Mater. Sci. 54 (2019) 6579–6585.
- [5] M.W. Kapp, C. Kirchlechner, R. Pippan, G. Dehm, Importance of dislocation pileups on the mechanical properties and the Bauschinger effect in microcantilevers, J. Mater. Res. 30 (6) (2015) 791–797.
- [6] R. Bandyopadhyay, S.E. Gustafson, K. Kapoor, D. Naragani, D.C. Pagan, M.D. Sangid, Comparative assessment of backstress models using high-energy X-ray diffraction microscopy experiments and crystal plasticity finite element simulations, Int. J. Plast. 136 (2021) 102887.

- [7] H. Mughrabi, Dislocation wall and cell structures and long-range internal stresses in deformed metal crystals, Acta Metall. 31 (9) (1983) 1367–1379.
- [8] O.B. Pedersen, L. Brown, W. Stobbs, The Bauschinger effect in copper, Acta Metall. 29 (11) (1981) 1843–1850.
- [9] E. Orowan, Internal stresses and fatigue in metals, in: Proceedings of the Symposium on Internal Stresses and Fatigue in Metals, Detroit, 1959.
- [10] A. Sleeswyk, M. James, D. Plantinga, W. Maathuis, Reversible strain in cyclic plastic deformation, Acta Metall. 26 (8) (1978) 1265–1271.
- [11] M. Kassner, P. Geantil, L.E. Levine, Long range internal stresses in single-phase crystalline materials, Int. J. Plast. 45 (2013) 44–60.
- [12] M. Kreins, S. Schilli, T. Seifert, A. Iyer, M.H. Colliander, S. Wesselmecking, U. Krupp, Bauschinger effect and latent hardening under cyclic micro-bending of Ni-base alloy 718 single crystals: Part I. Experimental analysis of single and multi slip plasticity, Mater. Sci. Eng.: A 827 (2021) 142027.
- [13] P.J. Armstrong, C. Frederick, et al., A Mathematical Representation of the Multiaxial Bauschinger Effect, Vol. 731, Berkeley Nuclear Laboratories Berkeley, CA, 1966.
- [14] W. Dettmer, S. Reese, On the theoretical and numerical modelling of Armstrong– Frederick kinematic hardening in the finite strain regime, Comput. Methods Appl. Mech. Engrg. 193 (1–2) (2004) 87–116.
- [15] L. Li, L. Shen, G. Proust, A texture-based representative volume element crystal plasticity model for predicting Bauschinger effect during cyclic loading, Mater. Sci. Eng.: A 608 (2014) 174–183.
- [16] M. Taylor, D. Agius, D. Knowles, M. Mostafavi, An investigation into the robustness of a crystal plasticity finite element model, in: Pressure Vessels and Piping Conference, Vol. 83860, American Society of Mechanical Engineers, 2020, V006T06A094.
- [17] S. Schilli, T. Seifert, M. Kreins, U. Krupp, Bauschinger effect and latent hardening under cyclic micro-bending of Ni-base alloy 718 single crystals: Part II. Single crystal plasticity modeling with latent kinematic hardening, Mater. Sci. Eng.: A 830 (2022) 142030.
- [18] R. Bandyopadhyay, S.E. Gustafson, K. Kapoor, D. Naragani, D.C. Pagan, M.D. Sangid, Comparative assessment of backstress models using high-energy X-ray diffraction microscopy experiments and crystal plasticity finite element simulations, Int. J. Plast. 136 (2021) 102887.
- [19] E. Demir, D. Raabe, Mechanical and microstructural single-crystal Bauschinger effects: Observation of reversible plasticity in copper during bending, Acta Mater. 58 (18) (2010) 6055–6063.
- [20] D. Ugi, K. Zoller, K. Lukács, Z. Fogarassy, I. Groma, S. Kalácska, K. Schulz, P.D. Ispánovity, Irreversible evolution of dislocation pile-ups during cyclic microcantilever bending, Mater. Des. 238 (2024) 112682.
- [21] D. Kiener, C. Motz, W. Grosinger, D. Weygand, R. Pippan, Cyclic response of copper single crystal micro-beams, Scr. Mater. 63 (5) (2010) 500–503.
- [22] E. Demir, A. Martinez-Pechero, C. Hardie, E. Tarleton, Restraining geometrically-necessary dislocations to the active slip systems in a crystal plasticity-based finite element framework, Int. J. Plast. (2024) 104013.
- [23] E. Demir, A. Martinez-Pechero, C. Hardie, E. Tarleton, OXFORD-UMAT: An efficient and versatile crystal plasticity framework, Int. J. Solids Struct. (2024) 113110.
- [24] E. Tarleton, Github link for crystal plasticity code, 2024, https://github.com/ TarletonGroup/CrystalPlasticity.
- [25] H.-J. Bunge, Texture Analysis in Materials Science: Mathematical Methods, Elsevier, 2013.
- [26] M. Smith, ABAQUS/Standard User's Manual, Version 6.14, Dassault Systèmes Simulia Corp, United States, 2022.
- [27] R. Hill, J. Rice, Constitutive analysis of elastic-plastic crystals at arbitrary strain, J. Mech. Phys. Solids 20 (6) (1972) 401–413.
- [28] E. Schmid, W. Boas, Kristallplastizität: Mit Besonderer Berücksichtigung der Metalle, Vol. 17, Springer-Verlag, 2013.
- [29] A.S. Khan, S. Huang, Continuum Theory of Plasticity, John Wiley & Sons, 1995.
- [30] B. Beausir, L.S. Tóth, K.W. Neale, Ideal orientations and persistence characteristics of hexagonal close packed crystals in simple shear, Acta Mater. 55 (8) (2007) 2695–2705.
- [31] Y. Huang, A User-Material Subroutine Incorporating Single Crystal Plasticity in the ABAQUS Finite Element Program, Harvard University, Cambridge, Massachusetts, 1991.
- [32] L. Gambirasio, G. Chiantoni, E. Rizzi, On the consequences of the adoption of the Zaremba–Jaumann objective stress rate in FEM codes, Arch. Comput. Methods Eng. 23 (2016) 39–67.
- [33] R. Hill, J. Rice, Constitutive analysis of elastic-plastic crystals at arbitrary strain, J. Mech. Phys. Solids 20 (6) (1972) 401–413.
- [34] W.L. Bond, The mathematics of the physical properties of crystals, Bell Syst. Tech. J. 22 (1) (1943) 1–72.

- [35] A.J. Cackett, C.D. Hardie, J.J. Lim, E. Tarleton, Spherical indentation of copper: Crystal plasticity vs experiment, Materialia 7 (2019) 100368, URL https://www.sciencedirect.com/science/article/pii/S2589152919301644.
- [36] F. Dunne, D. Rugg, A. Walker, Lengthscale-dependent, elastically anisotropic, physically-based hcp crystal plasticity: Application to cold-dwell fatigue in Ti alloys, Int. J. Plast. 23 (6) (2007) 1061–1083.
- [37] G.I. Taylor, Plastic strain in metals, J. Inst. Met. 62 (1938) 307-324.
- [38] A. Arsenlis, D. Parks, Crystallographic aspects of geometrically-necessary and statistically-stored dislocation density, Acta Mater. 47 (5) (1999) 1597–1611.
- [39] J.F. Nye, Some geometrical relations in dislocated crystals, Acta Metall. 1 (2) (1953) 153–162.
- [40] L. Meric, P. Poubanne, G. Cailletaud, Single crystal modeling for structural calculations: part 1—model presentation, 1991.
- [41] J. Chaboche, D. Nouailhas, Constitutive modeling of ratchetting effects—part I: experimental facts and properties of the classical models, 1989.
- [42] N. Ohno, J.-D. Wang, Kinematic hardening rules with critical state of dynamic recovery, part II: application to experiments of ratchetting behavior, Int. J. Plast. 9 (3) (1993) 391–403.
- [43] S.B. Brown, K.H. Kim, L. Anand, An internal variable constitutive model for hot working of metals, Int. J. Plast. 5 (2) (1989) 95–130, URL https://www. sciencedirect.com/science/article/pii/0749641989900259.
- [44] S. Kalidindi, C. Bronkhorst, L. Anand, Crystallographic texture evolution in bulk deformation processing of FCC metals, J. Mech. Phys. Solids 40 (3) (1992) 537–569, URL https://www.sciencedirect.com/science/article/pii/ 0022509692800039.
- [45] I.J. Beyerlein, C.N. Tomé, Modeling transients in the mechanical response of copper due to strain path changes, Int. J. Plast. 23 (4) (2007) 640-664.
- [46] E. Demir, D. Raabe, N. Zaafarani, S. Zaefferer, Investigation of the indentation size effect through the measurement of the geometrically necessary dislocations beneath small indents of different depths using EBSD tomography, Acta Mater. 57 (2) (2009) 559–569.
- [47] J. Nelder, R. Mead, A simplex method for function minimization, Comput. J. 7 (1965) 308–313.
- [48] A. Martinez-Pechero, Y. Zayachuk, A. Widdowson, D.E. Armstrong, E. Tarleton, Obtaining SiC fibers-PyC interfacial properties through push-out FEM models, J. Eur. Ceram. Soc. 44 (2) (2024) 784-794.
- [49] T. Vermeij, J. Wijnen, R. Peerlings, M. Geers, J. Hoefnagels, A quasi-2D integrated experimental–numerical approach to high-fidelity mechanical analysis of metallic microstructures, Acta Mater. 264 (2024) 119551.
- [50] A.T. Jennings, M.J. Burek, J.R. Greer, Microstructure versus size: mechanical properties of electroplated single crystalline cu nanopillars, Phys. Rev. Lett. 104 (13) (2010) 135503.
- [51] H. Dai, Geometrically-Necessary Dislocation Density in Continuum Plasticity Theory, FEM Implementation and Applications (Ph.D. thesis), Massachusetts Institute of Technology, 1997.
- [52] A. Sleeswyk, D. Verel, The rate-determining process in luders band growth, Scr. Metall. 6 (8) (1972) 677–679.
- [53] E. Demir, D. Raabe, N. Zaafarani, S. Zaefferer, Investigation of the indentation size effect through the measurement of the geometrically necessary dislocations beneath small indents of different depths using EBSD tomography, Acta Mater. 57 (2) (2009) 559-569.
- [54] S. Das, F. Hofmann, E. Tarleton, Consistent determination of geometrically necessary dislocation density from simulations and experiments, Int. J. Plast. 109 (2018) 18–42.
- [55] U. Essmann, U. Gösele, H. Mughrabi, A model of extrusions and intrusions in fatigued metals I. Point-defect production and the growth of extrusions, Phil. Mag. A 44 (2) (1981) 405–426.
- [56] K. Differt, U. Esmann, H. Mughrabi, A model of extrusions and intrusions in fatigued metals II. Surface roughening by random irreversible slip, Phil. Mag. A 54 (2) (1986) 237–258.
- [57] U. Essmann, H. Mughrabi, Annihilation of dislocations during tensile and cyclic deformation and limits of dislocation densities, Phil. Mag. A 40 (6) (1979) 731–756
- [58] H. Mughrabi, Cyclic slip irreversibilities and the evolution of fatigue damage, Met. Mater. Trans. B 40 (2009) 431–453.
- [59] E. Repetto, M. Ortiz, A micromechanical model of cyclic deformation and fatigue-crack nucleation in fcc single crystals, Acta Mater. 45 (6) (1997) 2577–2595.
- [60] M.D. Sangid, The physics of fatigue crack initiation, Int. J. Fatigue 57 (2013) 58–72.